A methodology for reactive transport modelling and geomechanical investigation of wellbores in CO2 storage sites

Bagheri, M., Shariatipour, S. M. & Ganjian, E.

Original citation & hyperlink:
Bagheri, M, Shariatipour, SM & Ganjian, E 2021, 'A methodology for reactive transport modelling and geomechanical investigation of wellbores in CO2 storage sites', Construction and Building Materials, vol. 268, 121100.
https://dx.doi.org/10.1016/j.conbuildmat.2020.121100

DOI 10.1016/j.conbuildmat.2020.121100
ISSN 0950-0618

Publisher: Elsevier

A methodology for reactive transport modelling and geomechanical investigation of wellbores in CO_2 storage sites

Mohammadreza Bagheri[a,*], Seyed M. Shariatipour[a], Eshmaiel Ganjian[b]

[a] Research Centre for Fluid and Complex Systems, Coventry University, Mile Lane, Coventry CV1 2NL, UK

[b] School of Energy, Construction and Environment, Built & Natural Environment Research Centre, Coventry University, Coventry CV1 5FB, UK

[*] Corresponding author, *E-mail address:* bagherim@coventry.ac.uk

Abstract

The movement of injected CO_2 from injection wells in CO_2 storage sites creates an acidic environment that comes into contact with the cement sheath with a possible consequential effect on its sealing performance. Thus the durability of the cement sheath can be threatened due to the degradation process and the stress state resulting from the new conditions found underground. The integrity of the cement sheath is a function of the cement composition, surrounding rock type, fluid pressure, stress state, temperature, and the type of well. This paper provides a methodology to investigate the stability of the rock-cement-casing assemblage. The assemblage's mechanical behaviour is coupled with the chemical alterations resulting from it being in contact with CO_2-bearing fluids. The cement matrix is a quasi-brittle material which shows a plastic behaviour. The character of the geomechanical part and the geochemical aspect mutually affects each other which is studied in this paper. A plastic-damage approach benefiting from the concept of embedded bands is also introduced to characterise the performance of the cement sheath within CO_2 storage sites. This approach considers both the failure and the deformation phenomena occurring within altered zones. In this paper, injection and abandoned wells are hypothesised at depths between 800-2500 m and their performance investigated. It is shown that abandoned wells are considered more likely to remain safe while the interfacial transition zones in injection wells are predicted to fail, which converts them to potential leakage pathways. Nevertheless, caution should be taken when the real wells are considered to match the required assumptions in the Introduction Section. In injection wells at depths of 1225-2500 m the cement-casing interface encounters pure dilation. However, the compaction process deforms the rock-cement interface at depths of 800-2500 m, which increases its durability again.

Keywords: CO_2 storage; Cement; Mechanics; Chemistry; Plastic-damage

1. Introduction

Any defects within the structure of abandoned or injection wells can potentially be converted into a CO_2 leakage pathways, as shown in Figure 1. These defects could be the result of exposure to CO_2-bearing fluids. The invasion of CO_2-bearing fluids into the cement sheath results in the formation of concentric zones with different chemo-mechanical properties [1–10]. Carbonation and degradation are the two main processes that occur throughout the exposure of the cement matrix to CO_2-bearing fluids. Portlandite (CH), as one of the main components of the cement matrix, is highly sensitive to the local pH value. As the pH decreases due to the initial diffusion of CO_2-bearing fluids into the cement matrix, the Portlandite starts to dissolve, leading to the formation of the Portlandite dissolution zone. Portlandite dissolution, as a part of the degradation process, leads to an increase in the porosity of the cement matrix and consequently reduces its strength [11,12]. The freed calcium cation from the Portlandite dissolution zone diffuses outwards (from deeper parts of the cement matrix towards the cement-brine interface) and precipitates at zones close to the cement-brine interface. This zone is referred to as the calcite precipitation zone, and the precipitation of calcite is referred to as the carbonation process. This process increases the strength of the cement matrix [13]. The renewal of CO_2-bearing fluids at the cement-brine interface diffuses higher quantities of carbon species into the cement matrix. Therefore, calcite, as the most stable form of calcium carbonate, starts re-dissolving in the CO_2-bearing fluids. Simultaneously, calcium silicate hydrate (C-S-H), within the outermost layers of the cement matrix, gradually degrades and calcium becomes depleted from this zone leaving behind a high porous silica gel. Calcium leaching from C-S-H and the re-dissolving of calcite are two chemical alterations that compose the second part of the degradation process occurring within layers close to the cement-brine interface [14]. The degradation process increases the porosity and reduces the cement strength within the degraded layers [6,13,15–20].

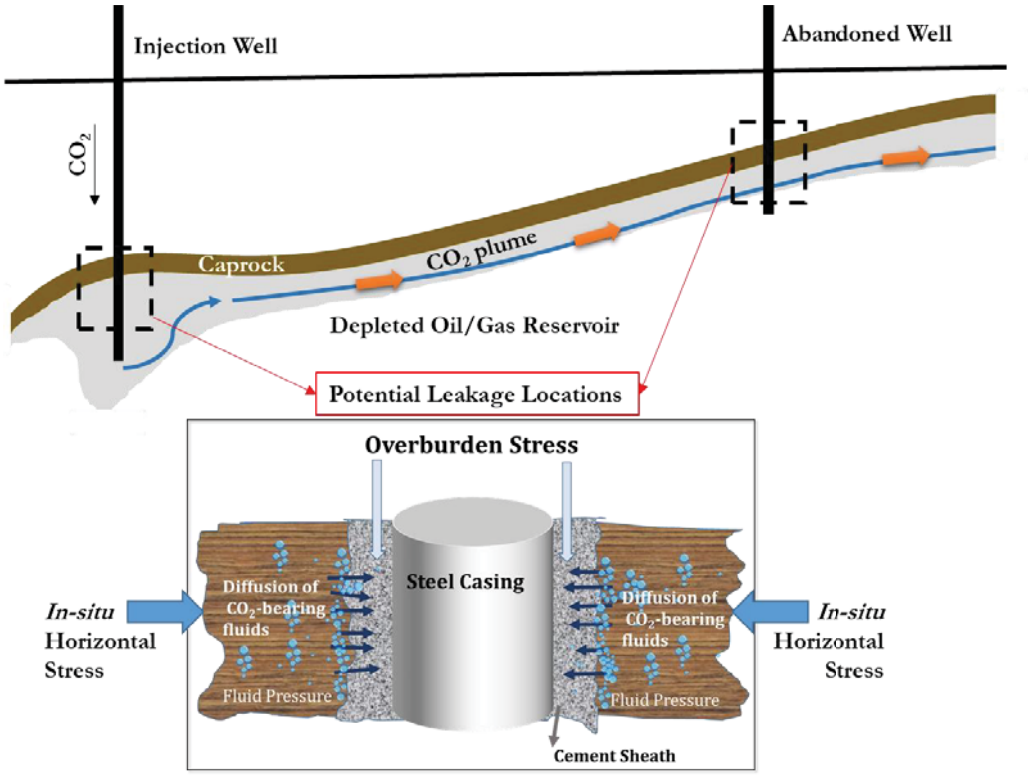

Figure 1. The movement of CO_2 plume and vulnerable locations to CO_2 leakage

It can be deduced that four main zones are formed as a result of the chemical reactions between the inner parts of the cement matrix and the cement-brine interface as follows [4,10,28,29,17,21–27]:

- An unaltered zone
- A Portlandite dissolution zone
- A calcite precipitation zone
- A silica gel zone or the C-S-H degradation zone

The rock-cement-casing assemblage also undergoes mechanical alterations due to the conditions found underground. Under high-temperature and high-stress conditions, a cement matrix could either fail or be deformed, particularly when it is in contact with an acidic environment. The failure of the cement sheath provides highly permeable pathways for CO_2-bearing fluids to escape, while any deformation limits existing leakage pathways. For example, McLean and Addis [30,31] introduced and applied a linear elasticity analysis to qualitatively model the stability of wellbores. Subsequently a more complex model was suggested by Yu et al. [32] to consider the effect of chemical alterations on the wellbore stability within the shale formations using the solute diffusion concept. Gholami et al. [33] investigated the integrity of the cement sheath using a thermo-poroelastic approach. For a production well, it was shown by Gholami et al. [34] that a reduction in the fluid pressure and non-uniform stress distribution around the wellbore leads to sand production and the deformation of the well casing. Moreover, the stress distribution at the wellbore could lead to the failure of either the casing or the cement sheath. However, the formation of failure cracks around the wellbore can be prevented by a high cohesive interface strength [35]. The

stress distribution and the cracking index are highly impacted by the tensile strength and the eccentricity, respectively [36]. Investigations on the stability of the cement sheath in other works, for example please refer [37–40], are also mostly focused on its mechanical alteration under high-pressure and high-temperature conditions rather than considering the chemical alterations as well. They provide a prediction on the integrity of the cement sheath under conditions found within active reservoirs or geothermal fields. Although many attempts have been undertaken towards the characterisation of wellbores, the behaviour of the rock-cement-casing invaded by CO_2-bearing fluids is still the subject of ongoing investigation.

In this paper, it is assumed that:

i. The cementing job has been perfectly conducted.
ii. None of the operations after the cementing job (for example, re-completion and perforating, etc.) has damaged the rock-cement-casing assemblage.
iii. The rock-cement-casing assemblage has not been damaged due to tectonic movements within its location.
iv. Well logs corresponding to the quality of the rock-cement-casing assemblage (such as cement bond logs, CBL) can confirm the vigour and health of wells in CO_2 storage sites prior to CO_2 injection.
v. The *in-situ* horizontal stress is not negligible.

In this paper, a methodology is developed to investigate the behaviour of the rock-cement-casing assemblage and is aligned with the previous work by the authors [29,41]. The behaviour of the cement matrix needs to be analysed in conjunction with the well casing and the surrounding rock. Two concepts of deformation and failure of the cement sheath will be represented. This work considers a plastic-damage approach coupled with the geochemical alteration; it also includes the behaviour of the interfacial transition zones (ITZ) where the cement sheath is in contact with the well casing and the surrounding rocks. The cement matrix shows a plastic behaviour under either compression or tension regimes. This behaviour could become activated at conditions found underground i.e., high-pressure and high-temperature environment. This is a likely phenomenon with considering that the cement matrix degrades under some specific conditions while exposed to CO_2-bearing fluids. In this paper, this behaviour will be investigated. The numerical approach for investigating the stability of the interfaces is based on the resolution of the boundary conditions, which is presented in the Supplementary material. The term rock will be used when a description is a general concept applied to both the rock and cement, and the cement specifically will be used to describe its unique properties.

The plastic-damage model is constructed based on the model presented by Xiao et al. [42] for modelling the uniaxial tension and compression tests. Triaxial models, such as the concrete damage-plasticity model 2 (CPDM2) developed by Grassl et al. [43], are also available for modelling the loading and unloading paths of the cement matrices. These models use almost ten constant parameters that the evolution of these parameters with respect to change in the chemical composition is not clear. In addition, their implementation needs to be conducted using the finite element method. To avoid the complexity and computational expense associated with models like CPDM2, the authors follow the uniaxial plastic-damage model

introduced by Xiao et al. [42] using a finite difference approach. Although the geochemical and geomechanical parts are validated separately in Section 7, the alteration in the parameters associated with characterising the failure envelope (such as compressive and tensile strengths and the Young's modulus) and porosity under stress is subject to more studies for it to be validated. The approach of coupling the geochemical with the geomechanical follows a sequential one-way approach in which the main outputs of the geochemical part are the porosity and the geochemical composition of the rock-cement-casing assemblage. They will be imported into the geomechanical part. In this part, the stability of the rock-cement-casing is investigated. Then, the new profile of porosity and the geochemical composition are re-imported into the geochemical simulation component. This cycle progresses until the rock-cement-casing assemblage fails. In this paper, the equations and parameters are common between the rock and the cement matrix unless the cement or the rock is particularly referred to. In Section 3, Eqs. (13)-(18) introduce the elastoplastic approach for the cement matrix. In Sections 4.3, Eqs. (33)-(35) and (38) are defined for the cement matrix and Eqs. (39)-(41) are especially developed for sandstone. Sections 5 and 6 pertain to the formation of bands in the cement sheath and its geochemical properties and alteration.

2. Basic mechanics

A cement matrix is similar to a porous rock, therefore the effective stress concept can be used to show the contribution of the fluid pressure on the distribution of stress within the porous media as follows [44–46]:

$$\sigma_{effective} = \sigma - \alpha p \tag{1}$$

where, $\sigma_{effective}$ is the effective stress, σ is the stress, α is the Biot coefficient, and p is the fluid pressure. In fact, the effective stress is the stress which is effective in moving or displacing soil [47]. The Biot coefficient is a function of the porosity and the rock type which changes from zero to close to one as porosity increases. The Biot coefficient can be calculated using the bulk modules of grains, K_s, and dry porous rock, K, respectively, as follows [48,49]:

$$\alpha = 1 - \frac{K}{K_s} \tag{2}$$

where,

$$K = \frac{E}{3(1-2\nu)} \tag{3}$$

$$K_s = \frac{E_0}{3(1-2\nu_0)} \tag{4}$$

E and ν are the Young's modulus and the Poisson's ratio of a porous rock, respectively. Here, it is assumed that E_0 and ν_0 are the Young's modulus and the Poisson's ratio of that rock when it is non-porous, respectively. As the value of bulk modules of grains, K_s, is larger than the bulk modules of dry porous rock, K, the Biot coefficient in Eq. (2) is less than one. For an isotropic porous media, in a cylindrical coordinate system, the normal stresses can be represented as follows [50–52]:

$$\sigma_r = \lambda'(\varepsilon_r + \varepsilon_\theta + \varepsilon_z) + 2\mu'\varepsilon_r + \alpha' p - (3\lambda' + 2\mu')\alpha_{CTE}\Delta T \quad (5)$$

$$\sigma_\theta = \lambda'(\varepsilon_r + \varepsilon_\theta + \varepsilon_z) + 2\mu'\varepsilon_\theta + \alpha' p - (3\lambda' + 2\mu')\alpha_{CTE}\Delta T \quad (6)$$

$$\sigma_z = \lambda'(\varepsilon_r + \varepsilon_\theta + \varepsilon_z) + 2\mu'\varepsilon_z + \alpha' p - (3\lambda' + 2\mu')\alpha_{CTE}\Delta T \quad (7)$$

where, σ_r, σ_θ, and σ_z are stresses in the r-direction, θ-direction, and z-direction, respectively. In the calculations in this paper, the compressive stress is assumed to be positive and the tensile stress is assumed to be negative. It is also assumed that the cement sheath is similar to a cylindrical system with a radial symmetry where the centre line coincides with the z-axis. It is worth noting that the fluid pressure only affects the normal stresses. ΔT is the temperature change and α_{CTE} is the coefficient of thermal expansion (CTE). α', λ' and μ' are the Biot coefficient, the Lame's constant, and the shear modulus for a damaged rock under either compression or tension regimes, which can be written as follows:

$$\alpha' = 1 - (1 - d_{tot})\frac{K}{K_s} \quad (8)$$

$$\lambda' = (1 - d_{tot})(K - \frac{2}{3}\mu) \quad (9)$$

$$\mu' = (1 - d_{tot})\frac{E}{2(1+\nu)} \quad (10)$$

where, μ is the shear modulus for an intact rock. d_{tot} is the total damage parameter which is a measure of the effective surface density of microdefects characterising the creation of microcavities [52].

In this paper, the plane strain condition is assumed to model the integrity of the cement sheath which is applied in literature [35,36,40,53,54].

3. Elastoplastic approach

The stress loading path affects the mechanical properties of the cement matrix. As a result, the stress distribution within the cement matrix is also a function of the loading path. Within the elastic area, the cement matrix will return to its initial state after unloading, while beyond the elastic boundaries the cement matrix will revert back to a different state from its initial one. In this case, the cement matrix will maintain a residual change compared to the initial state, which is referred to as the plastic-damage change. The stiffness of the cement matrix, however, is also affected due to either the matrix softening or hardening under the uniaxial tension or the compression loading path, respectively [42,55]. It was shown by Zhou et al. [56] that the cement sheath is more elastic at room temperature and is therefore more brittle. This behaviour changes to elastoplastic properties with increasing temperature in their experiments. It was reported that the risk of compressive failure increases with depth. Under these conditions, the cumulative residual strain increases, which implies the elastoplasticity [56]. To characterise oil well plasticity, Arjomand et al. [36] used a constitutive model developed by Lubliner et al. [57]. This model described the behaviour of the cement sheath under shearing at different levels of confinement. Generally, it can be understood that the behaviour of the cement matrix deviates from an elastic form with increasing pressure and temperature. This implies that an elastic approach is not enough to characterise the

behaviour of the cement sheath under conditions found underground. Therefore, an elastoplastic approach, that shows the mechanical behaviour of the cement sheath after failure or deformation, is required to model the stress-strain behaviour of the cement matrix in the inelastic area. This method determines the stress distribution beyond the elastic-plastic boundaries where the change in porosity is a crucial parameter for reactive transport calculations. In fact, elastic calculations are not valid beyond these boundaries and cannot be relied upon. In this paper, a plastic-damage model is proposed to include the alteration in the cement in areas beyond the elastic boundaries.

The plastic-damage model was introduced by Lubliner et al. [57] which was applied successfully to concrete. The cement matrix undergoes an elastoplastic evolution under cyclic loading. The development of microcracks results in a degradation of the stiffness [58] as the cement matrix is continuously changing. Based on this, the uniaxial constitutive expression of the plastic-damage model can be defined as:

$$\sigma = (1 - d)E : (\varepsilon - \varepsilon_p) \tag{11}$$

where, d is the damage parameter that characterises the profile of the uniaxial stress-strain relationship under both compressive and tensile loading paths. ε_p and ε_e are the plastic and the elastic composing parts of the strain, ε. The strain, ε, can be decomposed as:

$$\varepsilon = \varepsilon_e + \varepsilon_p \tag{12}$$

The quasi-brittle behaviour of the cement matrix needs more than one assumption in order to be characterised. The behaviour of the cement matrix under the axial tensile stress follows a monotonic profile [59]. Therefore, the damage parameters were introduced to show the evolution of the cement matrix stiffness. The strain equivalent principle (SEP) was applied to calculate the damage parameters as follows [42]:

$$d_t = \begin{cases} 0 & x_t \leq 1 \\ 1 - \dfrac{1}{a_t(x_t - 1)^{1.7} + x_t} & x_t > 1 \end{cases} \tag{13}$$

where,

$$x_t = \frac{\varepsilon}{\varepsilon_t} \tag{14}$$

and, d_t is tensile damage parameter for the uniaxial tensile stress-strain profile, a_t is a constant parameter, which is a function of strength and composition of the cement matrix, and ε_t is the strain of the cement matrix under a tension which is equal to the tensile strength of the cement matrix.

A monotonic stress-strain profile can also be used to characterise the behaviour of a cement matrix subjected to the axial compression [60–62]. The compressive damage parameter for the uniaxial compressive stress-strain profile was calculated using SEP [42] as follows:

$$d_c = \begin{cases} 0 & x_c \le x_1 \\ 1 - \dfrac{f_c}{E\varepsilon_c}(\alpha_c + (3-2\alpha_c)x_c + (\alpha_c - 2)x_c^2) & x_1 < x_c \le 1 \\ 1 - \dfrac{f_c}{E\varepsilon_c}\left(\dfrac{1}{\beta_c(x_c-1)^2 + x_c}\right) & x_c > 1 \end{cases} \quad (15)$$

where,

$$x_c = \frac{\varepsilon}{\varepsilon_c} \quad (16)$$

and, d_c shows the compressive damage parameter, x_1 is the ratio of the strain at the elastic-inelastic transition zone to the strain at which the stress equals the compressive strength of the cement matrix, ε_c. It should be noted that x_1 is smaller than x_c. α_c and β_c are two constants which are functions of the strength and the composition of the cement matrix, f_c is the uniaxial compressive strength (UCS) of the cement matrix. The values for a_t, α_c, and β_c are equal to 2.2905, 4.3154, and 0.9055, respectively, which are extracted from [58] on the monotonic uniaxial loading of a cement matrix. They are obtained by fitting Eqs. (13) and (15) to Figure 2 (a) and (b) in [58] for tensile and compressive stress, respectively. They are exclusively defined for the cement matrix. In this paper, those parameters are overlooked for the rock as it remains within the elastic zone.

As the cement matrix is under a three-dimensional stress state, a unique function therefore needs to be defined to combine the damage parameters into one scalar value of a total damage parameter, d_{tot}. The following shows d_{tot} as a function of d_c and d_t [55,58]:

$$d_{tot} = 1 - (1 - d_c)(1 - \bar{r}d_t) \quad (17)$$

where,

$$\bar{r} = \frac{\sum_{i=1}^{3}\langle\sigma_i\rangle}{\sum_{i=1}^{3}|\sigma_i|} \quad (18)$$

and, $\langle\sigma\rangle$ is the ramp function which is equal to $(\sigma + |\sigma|)/2$.

The total damage parameter, d_{tot}, is embedded in Eqs. (5)-(7) to include the plastic-damage behaviour of the cement matrix based on the proposed model. It should be noted that the plastic-damage model only describes the behaviour of the cement and the rock, and the well casing is assumed to remain within the elastic zone.

4. Plasticity yield and cap surfaces

The failure envelope is the union of the cap and yield surfaces, as shown in Figure 2. It shows the areas where the cement matrix is characterised using the elastic parameters. On approaching the elastic-inelastic boundaries, the total damage parameter increases. The shape of the failure envelope alters due to the undergone loading path, the change in the composition and mechanical properties of the cement matrix, and the stress state. The yield surface shows the boundaries where the dilation is active. The cap surface is assigned to the boundary, beyond which a compaction process occurs. Although Figure 2 is developed for the cement matrix, it also is practical to predict the behaviour of the rocks due to simultaneous effects of the geochemical and geomechanical alterations.

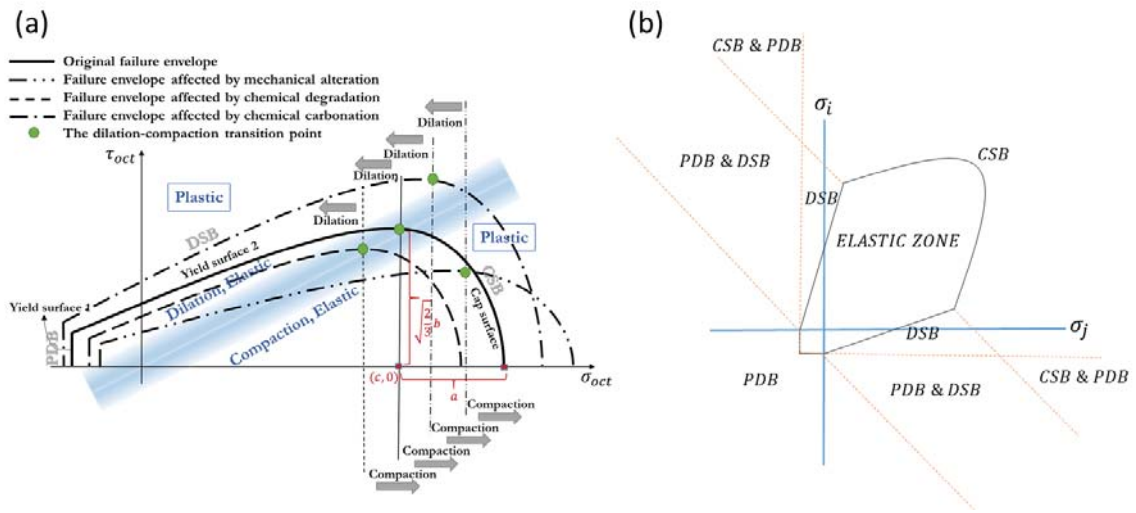

Figure 2. (a) Effect of the mechanical and chemical alteration on the failure envelope of the cement matrix. The abbreviations in this figure are defined as follows: PDB (pure dilation band); DSB (dilation shear band); CSB (compaction shear band); τ_{oct} (octahedral shear stress); σ_{oct} (octahedral normal stress); $(c, 0)$ is the line separating DSB from CSB; a and b are defined in Eq. (31) as the half-width and half-height for describing the elliptical cap surface; (b) The occurrence of different types of bands (PDB, DSB, and CSB) within a rock. σ_i and σ_j show the normal stress in the i and j directions, respectively.

Three forms of alteration within the cement matrix due to the burdened stress state are assumed in this work, shown by the yield surfaces 1, 2, and the cap surface in Figure 2.

4.1. Tensile failure

Yield surface 1 in Figure 2 is characterised by tensile failure. If the tensile stress on a rock exceeds its tensile strength, f_t, the rock will fail. This results in the formation of cracks with distinct surfaces which are perpendicular to the tensile stress. The tensile failure results in the softening of the rocks. The tensile failure can be predicted as follows [30,31]:

$$M = \min\{\sigma_r, \sigma_\theta, \sigma_z\} - \alpha p \tag{19}$$

where M is the minimum effective stress, then,

$$\eta_t = -\frac{M}{f_t} \tag{20}$$

The rock will fail under the tensile stress if the value of η_t as the tensile failure criterion increases to greater than one.

4.2. Shear failure

The shear failure is indicated by the Yield surface 2 in Figure 2. This type of failure is expected once the difference between the maximum stress, σ_1, and the minimum stress, σ_3, surpasses the shear strength of the rock [63]. Two cracks are probably formed due to the shear failure, where their imaginary interception line assumed to be parallel to the direction of the middle stress, σ_2. The shear failure results in the formation of either cracks or bands with a higher porosity compared to the intact zones within the rock. It is worth noting that the shear failure leads to softening. Although these bands are similar to the continuous transition zones between two intact zones, they are, however, not as distinct as the tensile failure cracks [64].

The Drucker-Prager criterion [65] is applied to describe the maximum shear strength of a rock. This criterion defines the yield surface 2 in Figure 2 which can be written as:

$$\tau_{DP} = \tau_0 + m(\sigma_{oct} - \alpha p) \tag{21}$$

where, τ_{DP} is the Drucker-Prager shear stress, which is the maximum shear stress that can be withstood by a rock, τ_0 and m are the intercept and slope of the Drucker-Prager criterion, respectively, depending on the internal friction angle, φ, and the cohesion, C, of a rock as follows [31]:

$$\tau_0 = \frac{2\sqrt{2}Ccos\varphi}{3 - sin\varphi} \tag{22}$$

$$m = \frac{2\sqrt{2}sin\varphi}{3 - sin\varphi} \tag{23}$$

The internal friction angle, φ, and the cohesion, C, of a rock can be written as functions of compressive strength, f_c, as follows [66]:

$$\varphi = \sin^{-1}\left(\frac{3}{1 + 0.4f_c/\sqrt{3}}\right) \tag{24}$$

$$c = (f_c - 5\sqrt{3})\frac{3 - sin\varphi}{6cos\varphi} \tag{25}$$

Octahedral normal stress, σ_{oct}, and octahedral shear stress, τ_{oct}, in Figure 2, are defined as:

$$\sigma_{oct} = \frac{I_1}{3} \tag{26}$$

$$\tau_{oct} = \sqrt{\frac{2}{3}J_2} \tag{27}$$

where, I_1 and J_2 are the first invariant of the stress tensor and the second invariant of the deviatoric stress tensor defined as follows:

$$I_1 = \sigma_r + \sigma_\theta + \sigma_z \tag{28}$$

$$J_2 = \frac{1}{6}((\sigma_r - \sigma_\theta)^2 + (\sigma_r - \sigma_z)^2 + (\sigma_\theta - \sigma_z)^2) + \tau_{r\theta}^2 + \tau_{rz}^2 + \tau_{\theta z}^2 \tag{29}$$

$\tau_{r\theta}$, τ_{rz}, and $\tau_{\theta z}$ are the shear stresses which are equal to zero due to the plane strain assumption and the symmetry of the cylindrical coordinate system which has been applied to demonstrate the rock-cement-casing assemblage.

Therefore, the shear failure criterion is as follows:

$$\eta_s = \frac{\tau_{oct}}{\tau_{DP}} \tag{30}$$

The rock will undergo shear failure if the shear failure criterion, η_s, exceeds one.

4.3. Deformation

With increasing octahedral normal stress, σ_{oct}, as defined in Eq. (26), the rock will be compacted due to the immense compressive stress loaded upon it. The compacted zones within the rock are bands with a reduced porosity compared to the other intact zones within the rock. In fact, within the compacted zones a rock will be deformed, which generally leads

to hardening. Therefore, no distinct planar surfaces are expected to be formed due to the compaction of the deformed zones. In this paper, the direction of these bands are assumed to be similar to the direction of shear failure bands.

The cap surface in Figure 2 shows the boundary of the elastic-compaction areas which is characterised by using an elliptical equation. The elliptical description for the cap surface is defined as follows [67–71]:

$$\frac{(I_1{}' - c)^2}{a^2} + \frac{J_{2cap}}{b^2} - 1 = 0 \tag{31}$$

where, I_1' is the effective first invariant of the stress tensor which is equal to $(I_1 - 3\alpha p)$ and J_{2cap} is the second invariant of the deviatoric stress tensor at the cap surface locus. The values of a, b, and c are shown in Figure 2. The deformation criterion can be defined as:

$$\eta_d = \begin{cases} \dfrac{J_2}{J_{2cap}} & c \le I_1 < (c + a) \\ \dfrac{I_1}{a} & I_1 \ge (c + a) \end{cases} \tag{32}$$

The deformation criterion, η_d, shows the tendency of a rock to be deformed due to the burdened stress state. The values for a, b, and c are obtained after some mathematical manipulation as follows, for the cement matrix [71]

$$X_2 = 17.087 + 1.892 f_{c,cement} \tag{33}$$

$$X_2 = c + a \tag{34}$$

$$r = 4.45994 \exp\left(\frac{-f_{c,cement}}{11.51679}\right) + 1.95358 \tag{35}$$

$$\alpha_1 = \sqrt{\frac{3}{2}}\tau_0 \tag{36}$$

$$\alpha_2 = \frac{m}{\sqrt{6}} \tag{37}$$

where, $f_{c,cement}$ is the uniaxial compressive strength of the cement matrix. Therefore, the value of c for the cement matrix is:

$$c = \frac{X_2 - r\alpha_1}{1 + r\alpha_2} \tag{38}$$

For the sandstone [67]

$$X_2 = 3 * 3663.85 \exp(-12.4\phi) \tag{39}$$

$$mc = 2\phi + 0.882 \tag{40}$$

And the value of c for the sandstone is:

$$c = \frac{X_2}{1 + \left(\frac{0.805}{mc}\right)^2} + 3\alpha p \tag{41}$$

The values of a and b for both the cement matrix and the sandstone can be calculated as follows:

$$a = X_2 - c \tag{42}$$

$$b = \alpha_1 + \alpha_2 c \tag{43}$$

5. Bands

The failure bands (both the tensile cracks and the shear failure bands) and deformation bands, in this paper, are translated altogether to bands. In fact, the bands are zones with either increased porosity, planar crack surfaces, or decreased porosity, as shown in Figure 3. Basically, the mineral composition of the bands is similar to the intact zones, unless affected by chemical reactions. The mechanical properties of the rock within the bands are different from the mechanical properties of the other intact zones. Porosity is the property of most concern regarding its effect on the mechanical properties, permeability, and diffusion coefficient. The mineral composition of a rock also influences the mechanical properties. Although the total damage parameter, d_{tot}, considers the effect of the plastic-damage evolution of a rock, it is not capable of quantifying the porosity change within failed or deformed zones. In this work, the concept of bands is considered as a method to be coupled with the elastoplastic approach to predict the porosity change within the affected zones. Three main band types are considered to represent all the affected zones as follows [64,72–79]:

- Pure dilation bands
- Dilation shear bands
- Compaction shear bands

Pure dilation bands (PDB) are defined as bands which are formed due to the tensile stress [74]. They have clearly distinct surfaces. Cracks can be considered as a subordinate to the PDB class. The porosity of the PDBs is one and they provide highly conductive pathways for fluids [80]. PDBs are perpendicular to σ_3 as the minimum stress resulting in the formation of cracks. Although the term tensile stress is applied to manifest the creation of PDBs, the hydraulic cracks are also a type of PDBs which are formed due to an increase in the fluid pressure, p. The yield surface 1 in Figure 2 represents the boundary beyond which PDBs will be formed. The maximum aperture, D_{max}, for PDBs can be calculated as follows [81]:

$$D_{max} = (\sigma_3 - \alpha p)\frac{1-\nu}{\mu}L \tag{44}$$

where, L is the crack length, σ_3 is the minimum normal stress, ν is the Poisson's ratio, μ is the shear modulus.

Generally, at middle values of compressive stress, and in the case of a significant difference between the values of σ_1 and σ_3, dilation shear bands (DSB) are formed. The Yield surface 2 in Figure 2 corresponds to the boundary between an elastic area and the area in which DSBs can potentially be formed. These bands increase the porosity within the affected areas [73,74,79]. The shape of the DSBs changes from the distinct planar surface i.e., cracks to zones which are continuous across the rocks with an increased porosity compared to the intact parts. The differentiation and the continuity between surfaces in DSBs depends on the size of $(\sigma_1 - \sigma_3)$ and σ_{oct}, respectively [64]. The larger $(\sigma_1 - \sigma_3)$, the more distinct will be the

separation of a rock at the DSBs. The larger σ_{oct} leads to an increase in the degree of continuity within the two imaginary planar dilation shear bands that are likely to be formed due to the stress state, in which their interception line will be parallel to the middle stress, σ_2. The low porosity of these bands limits the permeability and diffusion of fluids deeper into the rock [75,80].

The geometry of compaction shear bands (CSB) is assumed to be similar to the DSBs. CSBs are continuous bands across the rock with a porosity lower than the intact parts of the rock. These bands are classified as deformation due to the continuity of rocks within them. They can be distinguished from the failure bands (PDB and DSB) due to a decrease in the porosity. In contrast to the failure bands, CSBs are barriers preventing the invasion of fluids into the inner part of the rock [75,80]. The cap surface in Figure 2 shows the boundary beyond which the compaction process is active, resulting in the formation of CSBs.

As can be understood from Figure 2 and Eqs. (21) and (31), the DSB and CSB cannot co-exist within a rock. This is due to the dominance of octahedral shear and normal stresses on their behaviour. Therefore, under a stress state only one of the DSB or CSB can be assumed to be formed in a rock. PDBs are formed once the minimum stress becomes lower than the tensile strength of the rock, as represented in Eq. (19). This means that the formation of PDBs is a function of the minimum stress, σ_3. In fact, a rock can be under two significant compressive stresses of σ_1 and σ_2 while a tensile stress simultaneously acts due to σ_3 on one of the faces of the rock. This results in the formation of either PDB-CSB or PDB-DSB couples within the rock, depending on the values of σ_1 and σ_2 . The CSB-DSB couple, however, is never expected to be formed at the same time within the rock.

For DSBs and CSBs, the shear displacement, D_s, which is the displacement of two adjacent points in the affected zone of the rock along the shearing surface direction, can be expressed as [73]:

$$D_s = a_1 L^{b_1} \tag{45}$$

where, a_1 and b_1 are constants which depend on the rock type, in this paper, they are considered equal to 0.01 and 0.5, respectively. The thickness, T, of DSBs and CSBs can be calculated as [74]:

$$T = a_2 D_s^{b_2} \tag{46}$$

where, a_2 and b_2 are constants which are functions of the rock type. In this paper, they are considered to be equal to 3.13 and 1.54, respectively, extracted from [74].

The failure bands (PDB and DSB) increase the porosity and compromise the integrity of the rocks while deformation bands (CSB) improve their strength. The degradation in the mechanical strength of a rock is interpreted as a softening process resulting from weakening due to the formation of the failure bands. The yield surface of the rock shrinks due to the softening process. The deformation bands increase the mechanical strength of the rock, signifying the hardening process which expands the cap surface of the rock [72].

The density of the bands which are formed within the vulnerable parts of the rock-cement-casing assemblage is a function of the distance between the interfacial transition zones (ITZ)

and the affected parts. In fact, the ITZs are the casing-cement and the cement-rock interfaces. This definition of ITZ is adopted as an analogue to the fault to evaluate the bands' density, d_b, within the affected areas as microfractures, as follows:

$$d_b = a_3 \ln(x) + b_3 \tag{47}$$

where, x is the distance from the separation surface, a_3 and b_3 are two parameters which depend on the rock type and the porosity value. In this paper, they are assumed to be equal to -7.26 and 35.96, respectively. With increasing distance from the separation surface, Eq. (47) shows that the density of bands decreases in a logarithmic manner. This equation was adopted from the studies on the microfracture density by Faulkner et al. [80].

The porosity of rocks in the PDBs is equal to one due to the formation of cracks. DSBs show an increase of 8% in the porosity value compared to the intact parts of the rock. CSBs, in this paper, are assumed to be similar to cataclastic bands in which the porosity decreases by one order of magnitude [72]. Therefore, the porosity of bands can be outlined as:

$$\phi_{PDB} = 1 \tag{48}$$

$$\phi_{DSB} = 1.08\phi_0 \tag{49}$$

$$\phi_{CSB} = \phi_0/10 \tag{50}$$

where, ϕ_0 is the porosity of the affected zones prior to the formation of the bands. Therefore, the porosity of altered zones can be updated and used for the calculation of the stress distribution throughout the lifespan of the rock-cement-casing assemblage. The porosity evolution due to the formation of the bands can be formulated as follows:

$$\Delta\phi_b = \phi_{cm}(1 - \frac{1}{2\pi r\Delta r} + d_b W\phi_b) - d_b W\phi_b \tag{51}$$

where, Δr is the thickness of the radial layer at the radius of r, ϕ_{cm} is the porosity of that layer prior to the formation of the bands (or after imposing chemical alteration, and the elastic change), W is the width of the band which equals either D_{max} or T depending on the type of the band, and ϕ_b is the porosity of the band which can be equal to either of ϕ_{PDB}, ϕ_{DSB}, or ϕ_{CSB} , depending on the type of band. Figure 3 simply shows the method for calculating the porosity for a failed or deformed radial element. A failed or deformed radial element is composed of elastic parts following the porosity evolution based on the elasticity rules (i.e., Eq. (A.21) in supplementary data), and band parts wherein their porosity is calculated using Eqs. (48)-(50). The total impact of the alteration in the mechanical properties of the cement sheath is considered by d_{tot} in the Eqs. (5)-(7).

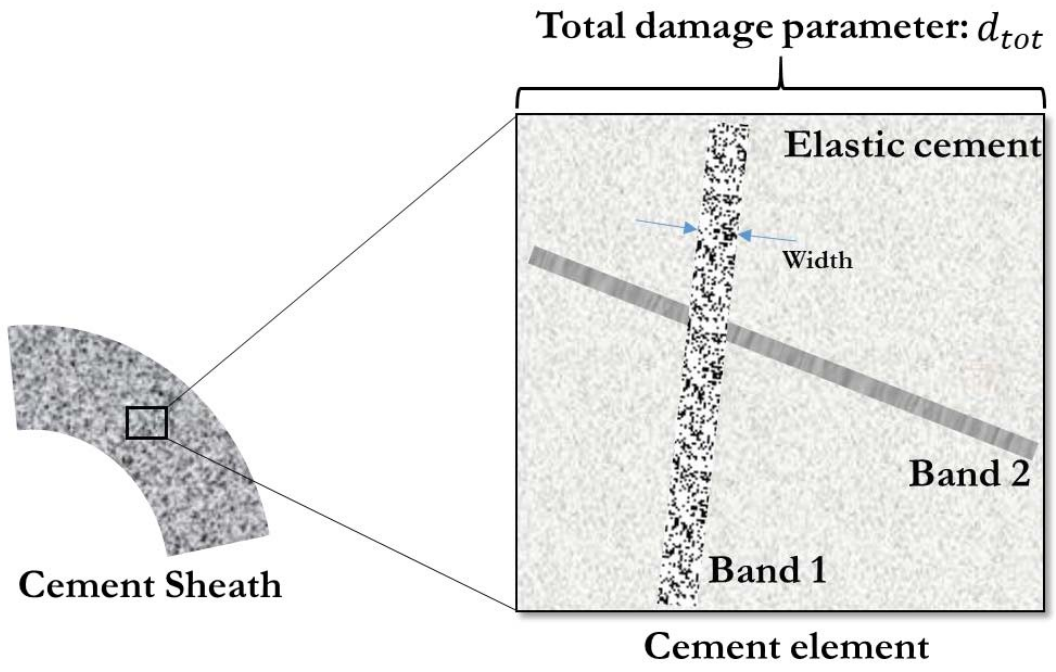

Figure 3. Porosity and Young's modulus of an element of the cement sheath after being exposed to CO_2-bearing fluids as a function of the elastic, failed, and deformed parts within the cement sheath element which can be defined as: $\phi_{element} = s_{band\ 1}\phi_{band\ 1} + s_{band\ 2}\phi_{band\ 2} + s_{elastic\ cement}\phi_{elastic\ cement}$, $s_{band\ 1} + s_{band\ 2} + s_{elastic\ cement} = 1$ & $s_i = V_i/V_{tot}$, and $E_d = E(1 - d_{tot})$.

6. Geochemistry

The invasion of CO_2-bearing fluids into the cement matrix results in either a degradation or carbonation process. The degradation process increases the porosity which leads to a decrease in the strength value. The failure envelope, as shown in Figure 2, shrinks compared to the original failure envelope. This implies that the cement matrix will be more fragile with respect to the burdened stress state. On the other hand, the carbonation process decreases the porosity within the affected areas which leads to an increase in strength [13]. Therefore, the failure envelope will expand, as shown in Figure 2, which implies an increase in the durability of the cement matrix.

The chemical alteration of a porous medium can be expressed as:

$$\frac{\partial\left(\phi S_\beta C_{j_\beta}\right)}{\partial t} = \nabla.\left(\phi S_\beta D^*_{j_\beta} \nabla C_{j_\beta}\right) - \nabla.\left(q_\beta C_{j_\beta}\right) + R_{j_\beta} + \zeta_{j\beta} + S_{j_\beta}, \quad (j = 1,2,3,\dots n) \tag{52}$$

where, ϕ is the porosity, S_β is the saturation of phase β, j refers to the composing components in the phase β, C_{j_β} is the concentration of the component j in the phase β, $D^*_{j_\beta}$ is the diffusion coefficient of the component j in the phase β, q_β is the velocity, R_{j_β} is the net produced/consumed rate of component j in the phase β due to the reactions happening within the porous media, $\zeta_{j\beta}$ shows the interphase transfer of component j from or into the

phase β, S_{j_β} is the mass transfer of component j between an external source and the phase β, and n is the number of the composing components in the phase β.

The CrunchFlow code was used to simulate the chemical alteration of the cement matrix. This code was developed by Steefel et al. [82] to simulate the geochemical alterations using energy, mass, and momentum conservation. The reactions that occur within the cement matrix can be classified into the precipitation and dissolution of minerals, and the reactions within the aqueous phase. The reactions between the solid and the aqueous phase (dissolution and precipitation) are kinetically controlled and are characterised by a reaction rate constant, k. Table 1 shows the reactions that occur within the pores of the cement matrix, and this table also represents the equilibrium constant, K_{eq}, for these reactions. Table 2 represents the reactions that occur between the solid and the aqueous phases, where, A_0 is the specific area, and α is the dependency of a reaction on H^+ activity. The reactions within the aqueous phase are fast and they are controlled by thermodynamic rules. These reactions are accounted for based on their equilibrium constant, K_{eq}.

The diffusion process is the main mass transportation phenomenon which is responsible for the invasion of carbon species both into and out of the cement matrix while the advection process renews CO_2-bearing fluids at the cement-brine interface [1,83–87]. The chemical alteration of the cement matrix can be either diffusion-limited [88] or reaction-limited [19,89,90] based on the difference between the reaction kinetics and the diffusion rate. In reaction-limited areas, the reaction fronts are closer to each other compared to the reaction fronts within the diffusion-limited areas [24,28]. The pure diffusion coefficients, D_0, of the aqueous species in the pore water of the cement matrix at a temperature of 50 ℃ are shown in Table 3.

Table 1. The reactions occurring in the aqueous phase and their equilibrium constants at 50 ℃ [15].

Aqueous phase reactions	Log (K_{eq})
$H_2O \leftrightarrow H^+ + OH^-$	-13.30
$CO_2(aq) + H_2O \leftrightarrow H^+ + HCO_3^-$	-6.09
$HCO_3^- \leftrightarrow H^+ + CO_3^{2-}$	-9.62
$CaCO_3(aq) \leftrightarrow Ca^{2+} + CO_3^{2-}$	-2.54
$CaCl^+ \leftrightarrow Ca^{2+} + Cl^-$	0.60
$CaCl_2(aq) \leftrightarrow Ca^{2+} + 2Cl^-$	0.59
$CaHCO_3^+ \leftrightarrow Ca^{2+} + HCO_3^-$	-1.11
$CaOH^+ \leftrightarrow Ca^{2+} + OH^-$	-0.45
$NaCl(aq) \leftrightarrow Na^+ + Cl^-$	0.73
$NaHCO_3^-(aq) \leftrightarrow Na^+ + HCO_3^-$	0.024

Table 2. The reactions describing either of the precipitation or the dissolution of minerals at 50 ℃ [15]. The Ca/Si ratio is 1.8 in this paper.

Reactions between the solid phase and the aqueous phase (precipitation and dissolution reactions)	**Log k ($\frac{mol}{m^2.s}$)**	**Log (K_{eq})**	**A ($\frac{m^2}{gr}$)**	**α**

$Ca(OH)_2(s)+2H^+ \leftrightarrow Ca^{2+}+2H_2O$	-6.20	21.05	16.50	0.18
$C\text{-}S\text{-}H(s)+3.6H^+ \leftrightarrow 1.8Ca^{2+}+7H_2O+SiO_2(am)$	-10.10	32.60	45.00	0.33
$CaCO_3(s) \leftrightarrow Ca^{2+}+CO_3^{2-}$	-6.10	-8.11	1.00	0.08
$SiO_2(am) \leftrightarrow SiO_2(aq)$	-10.00	-2.54	1.00	0.00

In this work, it is assumed that CO_2 is completely dissolved in brine and it never escapes from the dissolution throughout the lifespan of the cement matrix. This assumption is reliable because CO_2-bearing fluids reaching the wells, particularly abandoned ones, have a lower level of dissolved CO_2 compared to the maximum soluble CO_2 calculated from thermodynamic rules [91,92]. In addition, at deep locations within underground formations the fluid pressure and temperature are above the critical pressure, 7.38 MPa, and temperature, 31.1 ℃, of CO_2, respectively. Therefore, CO_2 will be in the supercritical state. This process fortifies the assumption considering the complete dissolution of CO_2 in brine. Based on this the single dominant aqueous phase is the only assumed fluid phase within the pores of the cement matrix and the pores near to the cement-rock interface.

Table 3. Diffusion coefficient of the aqueous species in water at 50 ℃ [15,20].

Species	D_0 (10^{-5} $\frac{cm^2}{s}$)
H^+	15.9
Ca^{2+}	1.36
OH^-	9.01
Cl^-	3.47
HCO_3^-	2.02
CO_3^{2-}	1.63
$CO_2(aq)$	3.21
$SiO_2(aq)$	1.86
Na^+	2.27
Other species	1.00

7. Verification of methodology

The modelling approach is based on the integrity status and the value of the radial stress at the locations of the ITZs. Nine boundary conditions are possible to dominate the rock-cement-casing assemblage. In this paper, a series method is applied to couple the geomechanical calculations with the geochemical alterations using the dominating boundary conditions. The works by Omosebi et al. [93] and Ahmed et al. [94] provide insightful investigations on the alteration of the cement matrix in high-pressure and high-temperature environments. In their work, they conducted experiments and modelled the degradation of the cement matrix from both the geochemical and the geomechanical points of view before and after exposure to CO_2-bearing fluids. In comparison to their work, in this paper the simultaneous effects of the geochemical and geomechanical alterations on the integrity of the rock-cement-casing assemblage is modelled. This method applies a plastic-damage model to simulate the behaviour of the cement sheath. In Supplementary material for this paper, it is shown that the boundary conditions alter with time for the rock-cement-casing assemblage. Therefore, a resolution of the boundary conditions which characterises the rock-cement and cement-

casing interfaces are introduced in the Supplementary material. This method is explained in detail which can be found in Supplementary material for this paper.

The method developed in this paper is composed of two main sections of chemical and mechanical calculations. As the fluid pressure and the temperature is considered higher than the critical pressure and temperature of CO_2, respectively, it will be in the supercritical state. On the other hand, it is also assumed that CO_2 is completely dissolved in brine and all the pores of the cement matrix are filled with single-phase fluids. This results in the chemical reactions being independent of the mechanical calculations. Therefore, this could justify using an iterative approach for coupling the chemical and the mechanical alterations. The alteration of the cement sheath as the only existing solid phase which is exposed to CO_2-bearing fluids was modelled in the work of Bagheri et al. [29]. Their method was aimed at modelling two probable phenomena of the radial cracking and the compaction within the affected layers of the cement sheath. Both the propagation of the cracks and the compaction of outer layers close to the cement-rock interface were investigated. They reproduced the penetration depth of the chemical reaction fronts which were reported in the works of Kutchko et al. [25] and Liteanu and Spiers [95]. Their work showed a reasonable agreement with the penetration depth of the reaction fronts.

This work provides an explicit methodology explaining the occurrence of each phenomenon as a function of the conditions found underground. This methodology models the behaviour of the entire rock-cement-casing assemblage. Mito et al. [96] conducted an experiment on the rock-cement-casing assemblage to explore the integrity of a well exposed to either CO_2 or N_2 under wet, saturated, and wet-saturated conditions. They exposed the well cement samples to supercritical CO_2, CO_2-saturated brine, and both CO_2 and CO_2-saturated brine. Figure 4 (a) shows that a cylindrical rock-cement-casing assemblage was prepared to imitate an abandoned well. API Grade J-55 cement was chosen for the casing. A cement slurry was prepared by mixing Ordinary Portland cement with water according the ratio 1/0.46 for making Class A cement suggested by the American Petroleum Institute [97]. The prepared samples were cured in pure water under room conditions for three days. Three samples were placed in a pressure vessel as shown in Figure 4 (b). The uppermost sample was in contact with water-saturated supercritical CO_2, the bottom-most was in contact with CO_2-saturated brine, and the middle one was in contact with both wet CO_2 and CO_2-saturated brine. The batch experiments were run for a duration of 3, 14, 28, and 56 days. The pH value was monitored during the experiments. After each experiment the inner part of the samples were imaged. The elemental mapping, the pore structures, and the chemical composition of the samples were analysed, and a detailed mineralogical determination was also performed. Table 4 shows the main inputs for simulating the CO_2-saturated experiments conducted in [96]. The initial composition, UCS, uniaxial tensile strength (UTS), and the Young's modulus are calculated using Section A.1.1 in supplementary data for this paper.

Table 4. Properties for simulating the CO_2-saturated experiment of Mito et al. (2015).

Property	**Value**
Fluid Pressure	10 MPa
Temperature	50 ℃

Salinity of brine	0.5 M NaCl
Fluids phase	CO_2-saturated brine
Duration	56 days
Diameter of solid carbon steel bar (J-55 casing material)	4 mm
Outer diameter of the cement sheath (Class A)	13 mm
Outer diameter of rock (Tago sandstone)	30 mm
Assumed initial porosity for cement	0.15
Assumed initial porosity for rock	0.22

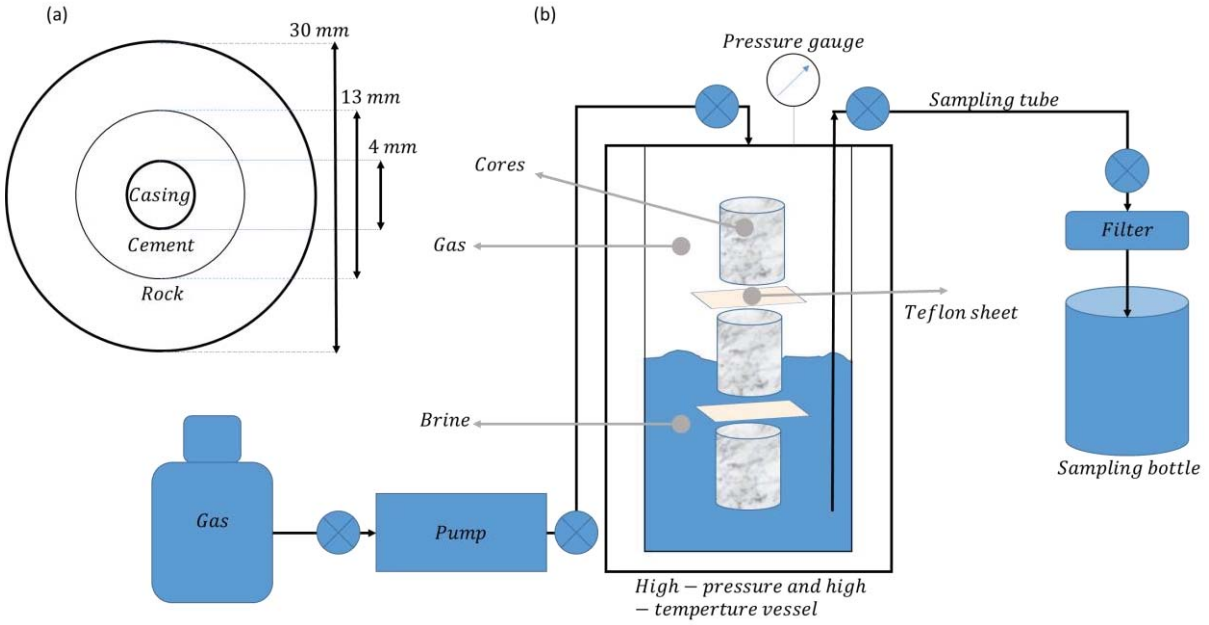

Figure 4. (a) A representation of the rock-cement-casing assemblage dimensions and (b) the experimental set up by Mito et al. [96].

Figure 5 shows the alteration depth in the cement sheath reproduced using the methodology represented in this paper versus the experimental values reported by Mito et al. [96]. The alteration depth in Figure 5 is defined as the distance from the cement-rock interface to where the porosity value decreases to below 0.14. This is the location within the cement sheath where calcite gradually begins to precipitate. The Portlandite dissolution is responsible for an increase in the porosity, although this process occurs at deeper locations within the cement sheath. The porosity change due to the Portlandite dissolution is not comparable with the effect of the calcite precipitation on the porosity. The studies in this paper and in the works of Bagheri et al. [29] confirm that the Portlandite dissolution covers an extensive area which is deeper than the calcite precipitation zone. This is due to the high sensitivity of Portlandite to the reduction of pH. It was observed that the calcite precipitation zone generally is a thin layer at shallower depths of the cement sheath limiting the diffusion of more carbon species into the cement sheath. As can be seen from Figure 5, the simulation results are in acceptable agreement with the experimental data.

In this simulation, the carbonation depth is defined as the location within the cement sheath where the porosity is reduced to a minimum value. Carbonation results in the formation of calcite reducing the porosity and increasing the strength [13]. To simulate the carbonation depth reported by Mito et al. [96], the minimum porosity is associated with the highest calcite precipitation where the porosity becomes lower than 0.10. The simulated carbonation depth in Figure 6 provides a satisfactory prediction for the experimental data reported by Mito et al. [96].

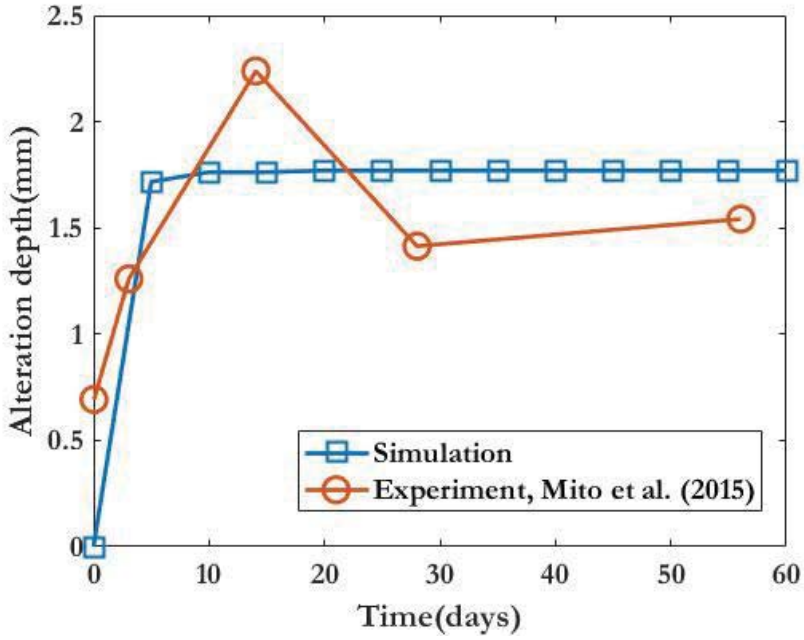

Figure 5. The alteration depth of the cement sheath from the experiments in [96] versus the simulated alteration depth.

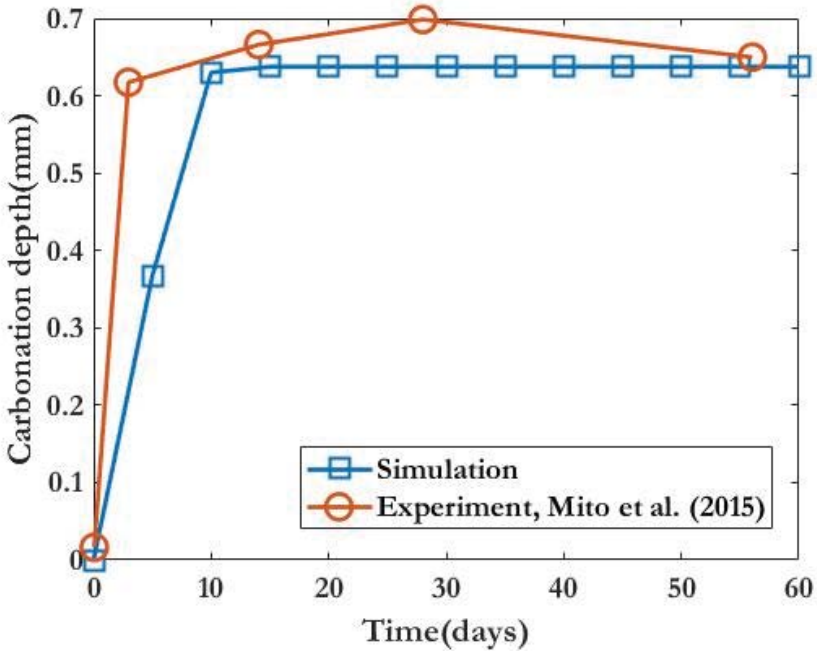

Figure 6. The ingress of the carbonation front into the cement sheath from the experiments in [96] compared to the predicted carbonation depth.

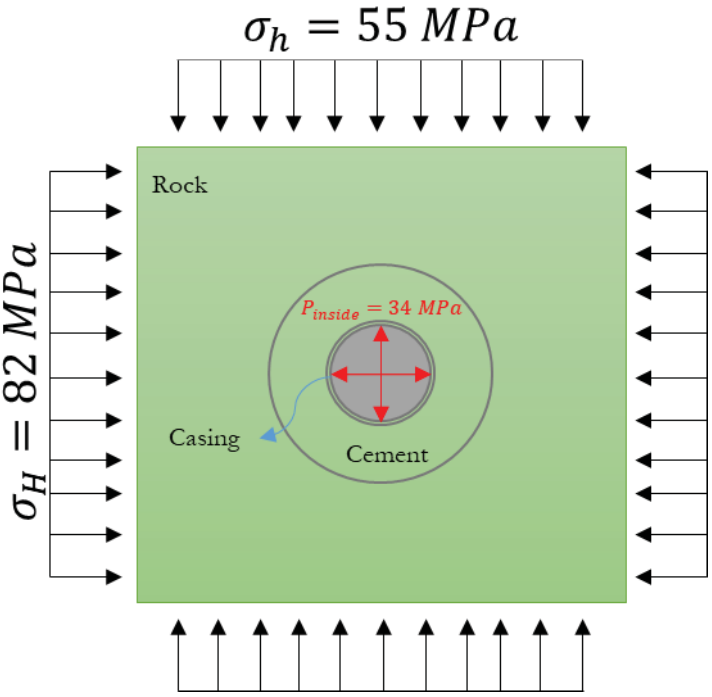

Figure 7. The stress state considered in [98].

Liu et al. [98] investigated their analytical model developed for the calculation of the stress field in the rock-cement-casing assemblage. They verified their analytical models by comparison to the results obtained from finite element analysis (FEA) as the numerical method which is widely applied for tackling complex geometries. In this paper, the FEA results in [98] are also used to examine the validity of the part for the geomechanical simulation. The geometrical and mechanical properties are outlined in Table 5, and the rest of the input properties are assumed to be similar to the information given in Section A.1.1. As shown in Figure 7, the inside pressure is equal to 34 MPa, the *in-situ* horizontal stress at 0° direction is 82 MPa, and the *in-situ* horizontal stress at 90° direction is 55 MPa. Finite element analyses in [98] were conducted considering two states of boundaries, including fixed boundaries referred to as the surface pressure state and the boundaries which are far away from the cement-rock interface referred to as the initial stress state in Figure 8. As the model presented in this paper is developed based on the surface pressure state, it can be observed that the behaviour of this model is close to the FEA-surface pressure curves in Figure 8. Our model is run at both the *in-situ* horizontal stresses of 55 and 82 MPa in order to compare it with the results presented in [98]. It can be seen that the reproduced σ_θ curves match the published results within the cement and rock areas to a reasonable degree, while σ_r shows a considerable difference close to the casing-cement interfaces. This is due to the cylindrical boundary assumed in this paper compared to the boundaries in [98] as shown in Figure 7.

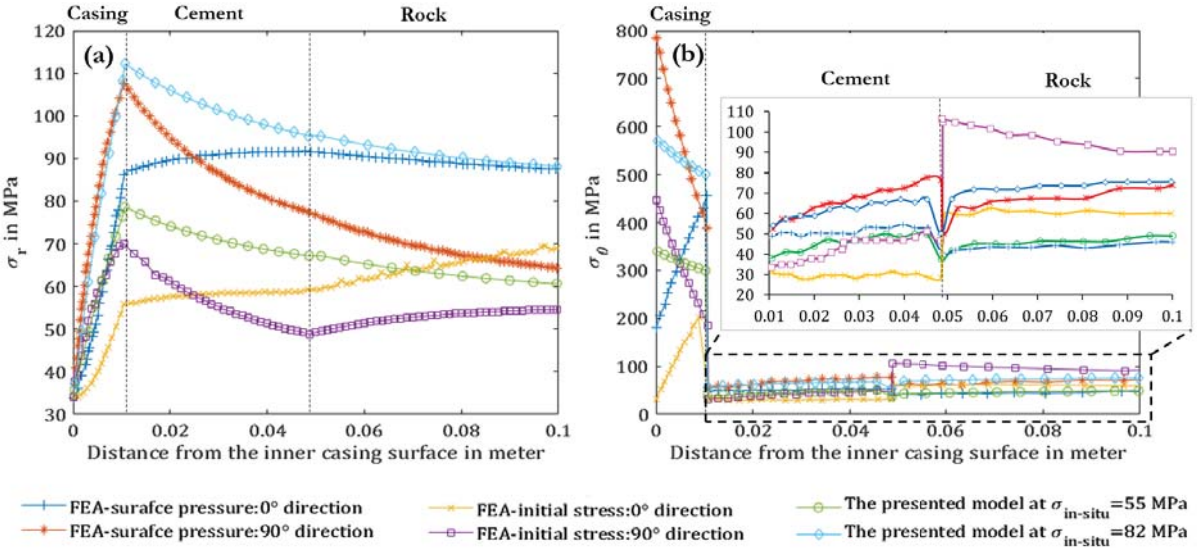

Figure 8. Comparison of the profile of the stress distribution in (a) the r-direction, and (b) θ-direction with the results presented in [98].

Table 5. Input properties for the model of [98].

Component	Young's modulus (GPa)	Poisson's ratio	Inner radius (mm)
Casing	210	0.30	59.31
Cement	12	0.25	69.85
Rock	10	0.20	107.95

To the authors' knowledge, there is a dearth of information pertaining to the tri-axial loading on the rock-cement-casing assemblage while they are under the effect of CO_2-bearing fluids. Therefore, the verification of the methodology presented in this work is subject to further experimental studies. Nevertheless, this section shows that the modelling approach provides a reasonable prediction for the alteration and carbonation depths. With the exception of the data and properties which are provided in this section, and in the Table 4 and Table 5, the remaining properties of the cement and the rock are presented in the Supplementary material.

8. Results and discussion

In this section, the alteration of the rock-cement-casing assemblage is investigated for two hypothetical cases. The first case considers an abandoned well which is exposed to CO_2-bearing fluids, and in the second case, an injection well is investigated which has been left following 2.5 years of CO_2 injection. Both cases cover a five-year period, and the ultimate lifespan of the ITZs and the cement sheath are predicted based on the extrapolation of their performance in this period. This is due to the high computational demands required to simulate time periods of more than 1000 years. In addition, this approach prevents increasing trends in the truncation and the round-off errors which make outputs unreliable.

8.1. Abandoned well

Under abandonment conditions, wells have been left dried or inactive. The temperature of an abandoned well reaches an equilibrium with the surrounding formation with time. It can be considered to be equal to the temperature of the surrounding formations calculated using Eq. (A.11) in supplementary data which is a function of the depth. For an abandoned well the pressure on the inside wall of the well casing is equal to 2.95 MPa, as explained in Section A.1.1.7. This pressure is equal to the hydrostatic pressure of a 274-m column of mud with the density of 1.097 gr/cm^3 (or 11 lb/gal) above the plug exactly set beneath the caprock. The interfacial transition zones are the most vulnerable zones subject to alteration due to their lower UCS and UTS compared to the other zones within the rock-cement-casing assemblage. On the other hand, as the cement sheath is assumed to be the only reactive solid phase with lower UCS and UTS compared to the rock and casing, it will be more susceptible to alteration. Therefore, the behaviour of the ITZs and the cement sheath have been studied throughout a five-year time period.

Figure 9 shows that the casing-cement interface is not affected by the invasion of CO_2-bearing fluids over five years. The extrapolation of graphs in Figure 9 exhibits an indefinite lifespan for the casing-cement interface for an abandoned well. The cement-rock interface is compacted after being exposed to CO_2 bearing fluids, as shown in Figure 10 (c). The compaction of the cement-rock interface prevents CO_2 escaping vertically towards the upper formations. It also limits the invasion of carbon species into the deeper parts of the cement sheath. This phenomenon occurs due to a decrease in the porosity of the cement-rock interface. The cap surface shrinks due to the degradation of the outermost layers of the cement sheath. This process results in the stress state becoming located within the inelastic-compaction area, as shown in Figure 2. It should be noted that the deformation resulting from the compaction process does not increase the strength of ITZs, because it is assumed that the cohesive strength of two materials is a function of their chemistry rather than their mechanical properties. The comparison of Figure 10 (a) with Figure 10 (c) signifies that an element could not simultaneously experience the formation of DSB and CSB. The behaviour of the entire cement sheath is similar to the casing-cement interface, as shown in Figure 11. This is due to the compaction of the cement-rock interface and the carbonation process at depths close to the cement-rock interface limiting the invasion of CO_2-bearing fluids into deeper parts of the cement sheath. Consequently, a significant part of the inner layers of the cement sheath and the casing-cement interface will be protected from CO_2 attack.

The layers of the cement sheath degrade due to the gradual dissolution of Portlandite. These layers remain within the elastic zone and the change in the stress distribution is negligible. After a while, the elastic compaction of the mildly degraded layers increases the strength again. Therefore, a reduction and then an increase in the strength within the elastic zone forms the fluctuation in Figure 9 (a-b) and Figure 11 (a-b). These fluctuations shift towards longer time intervals with decreasing in depth, due to the low concentration of CO_2 at shallower depths resulting from the low fluid pressure. This means that the pH of CO_2-bearing fluids is lower, thus they have a lower capability of making an impact on the cement sheath. It can be deduced from Figures 9-11 that abandoned wells will retain their integrity for an indefinite length of time. Although the trends of curves in Figures 9-11 cannot be detected

easily due to the large scale of y-axis, the lifespans of the ITZs and the cement sheath are calculated using the extrapolation of those trends as shown in Figure 12. This figure simply shows that the cement-rock interface of the abandoned well is compacted once the CO_2-bearing fluids invaded the cement sheath. It can be observed that the rock-cement-casing assemblage remains intact.

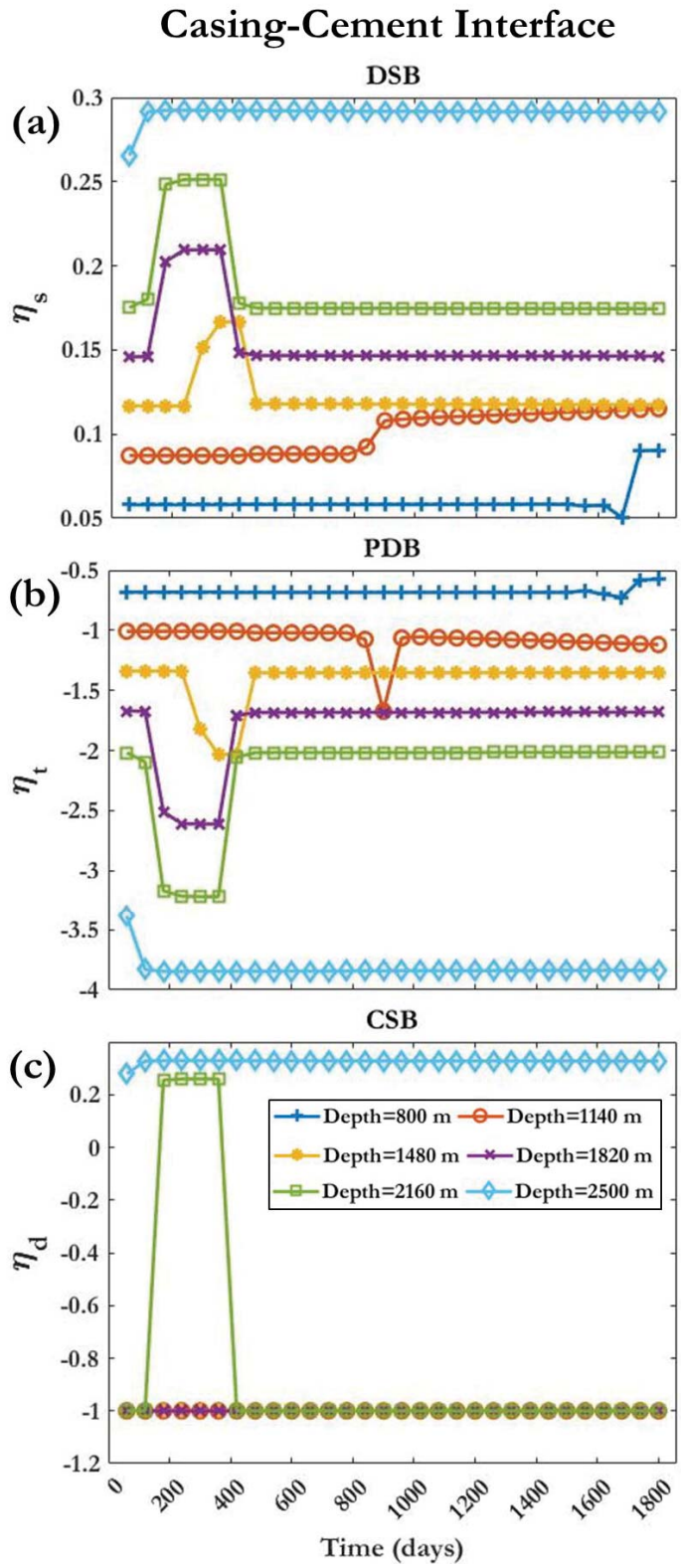

Figure 9. (a) Change in the value of the shear failure criterion, η_s; (b) the tensile failure criterion, η_t; (c) and the deformation criterion, η_d, at the different depths for the casing-cement interfacial transition zone under the abandonment conditions.

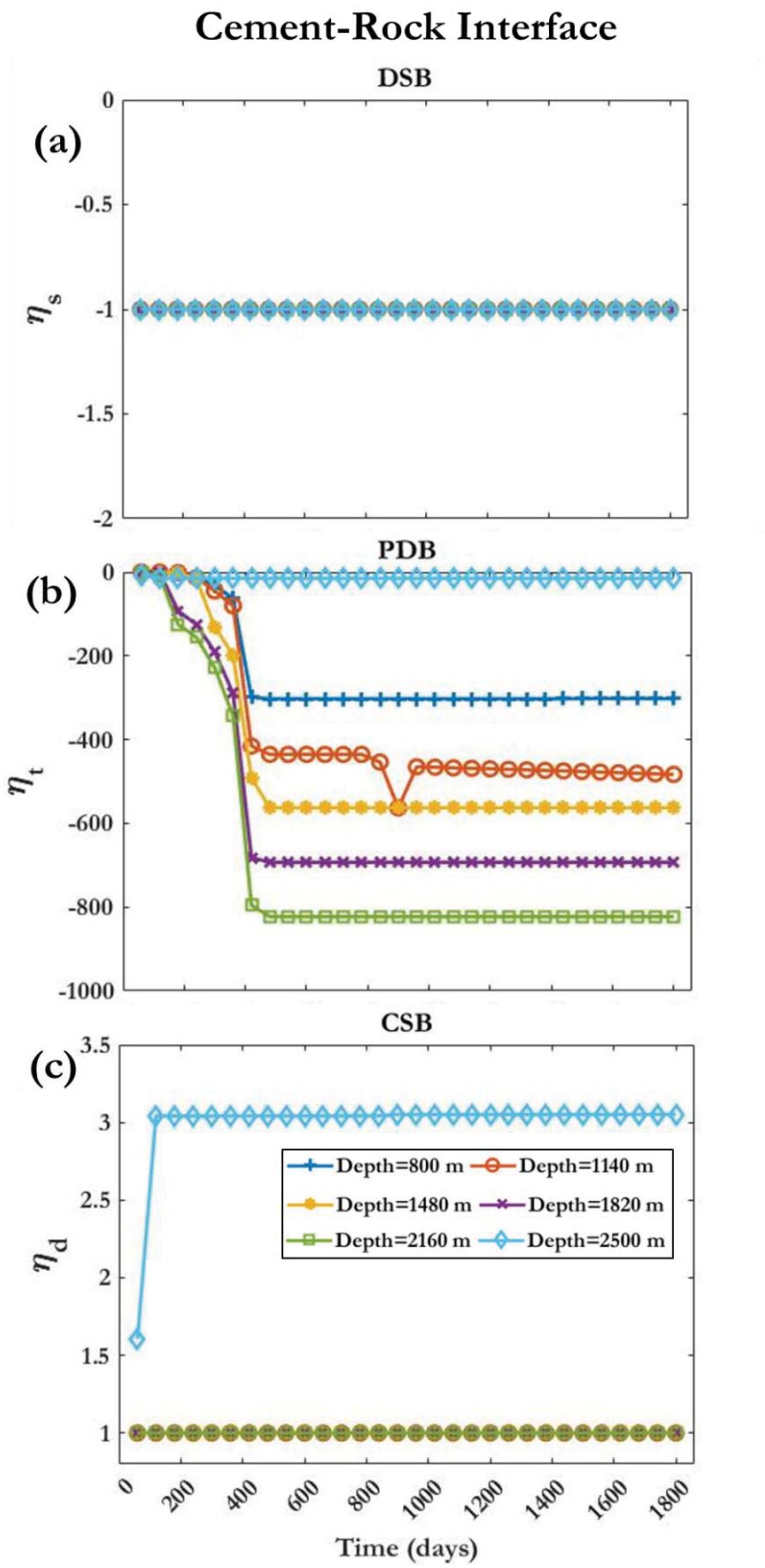

Figure 10. (a) Change in the value of the shear failure criterion, η_s; (b) the tensile failure criterion, η_t; (c) and the deformation criterion, η_d, at the different depths for the cement-rock interfacial transition zone under the abandonment conditions.

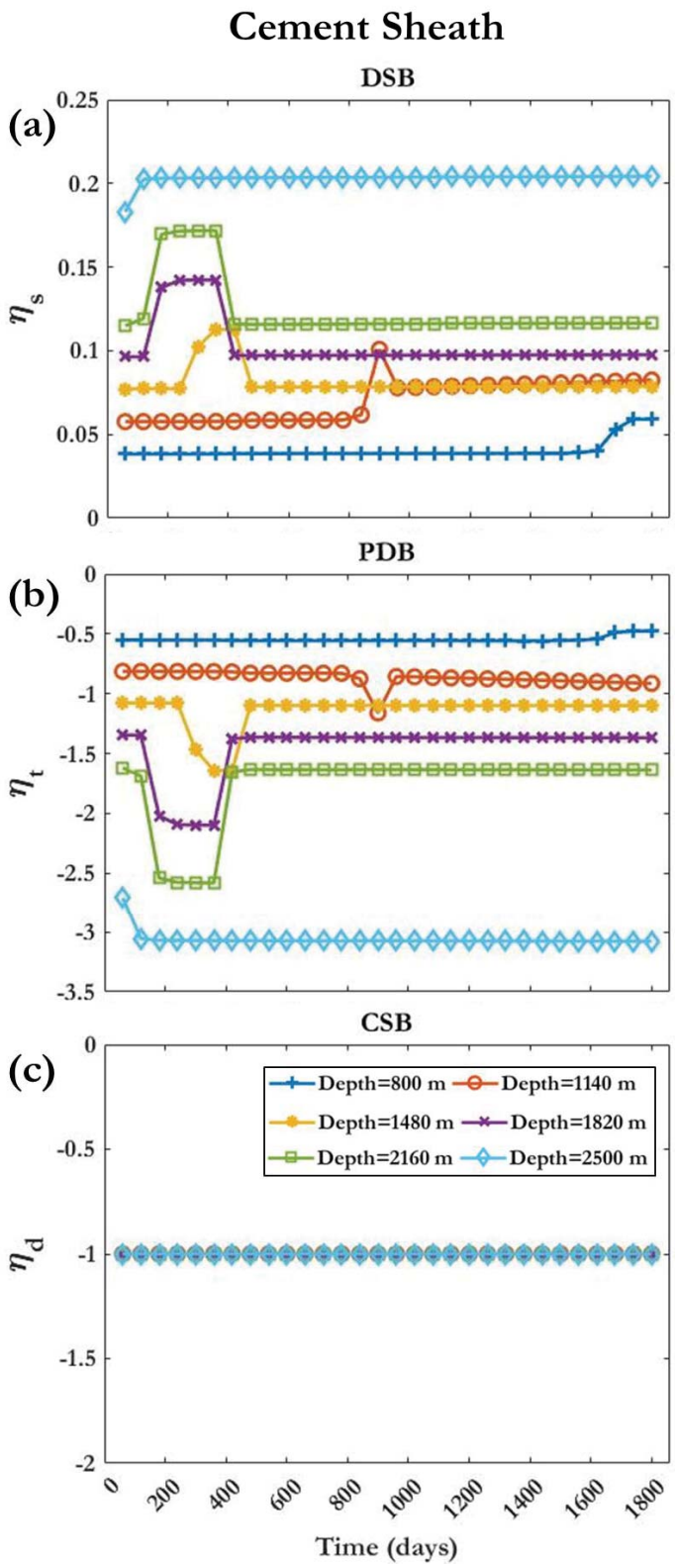

Figure 11. (a) Change in the value of the shear failure criterion, η_s; (b) the tensile failure criterion, η_t; (c) and the deformation criterion, η_d, at the different depths for the entire cement sheath under the abandonment conditions.

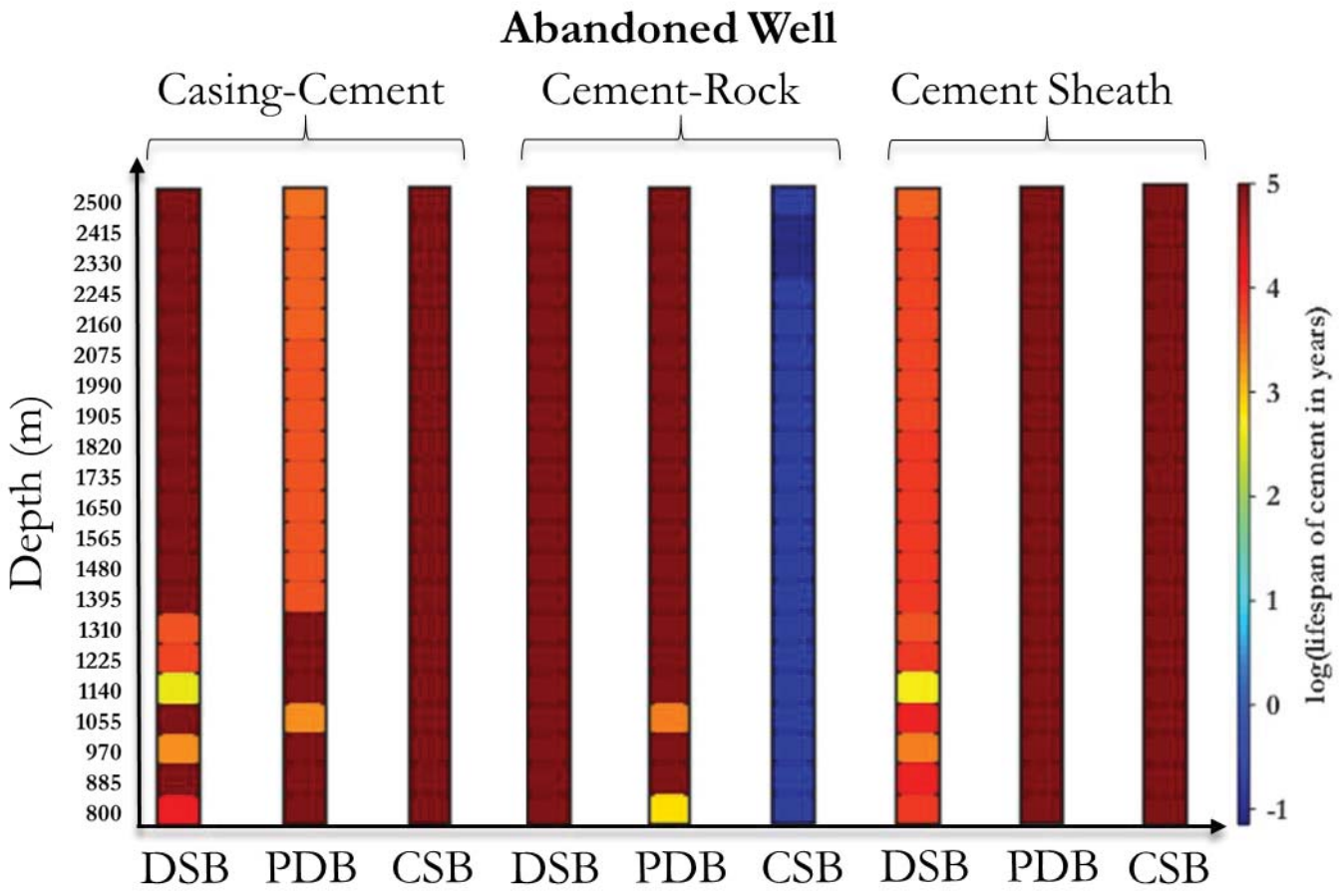

Figure 12. The lifespan of the casing-cement and cement-rock interfaces, and the cement sheath for an abandoned well.

8.2. Injection well

Table 6 explains the alteration of the ITZs at the time step of zero for Figure 13 and Figure 14. Figures 13-15 represent the alteration in the failure and the deformation criteria for a well which has been used as a CO_2 injection well for 2.5 years, and then the injection process stopped, and the well plugged and abandoned. During the injection period, the inside temperature is considered to be 30 ℃. After plugging, the temperature in the well again reaches an equilibrium with the surrounding formations.

As outlined in Table 6, once CO_2 is injected (i.e., the time step of zero) at deeper points of a well the casing-cement interface will fail due to the tensile stress created by a reduction in the temperature. The temperature inside the well drops from the formation temperature to the CO_2 injection temperature of 30 ℃. This decrease leads to the creation of a tensile stress at the casing-cement interface. In fact, both the casing and the cement sheath start contracting with the decrease in temperature. The coefficient of thermal expansion for the cement and the casing are different, thus their volume contraction at the cement casing would not be the same. This phenomenon leads to a tension at the casing-cement interface. Based on Eq. (A.15) the uniaxial compressive strength of the cement-casing is a fraction of that strength for the cement sheath. Consequently, the uniaxial tensile strength is also lower than that value for the cement sheath. This signifies that in the presence of a tension the casing-cement interface will be more prone to failure rather than the cement sheath.

The cement-rock interface retains its integrity at time step zero except at a depth of 2500 m where it fails due to shear stress. The shear failure of the cement-rock interface at a depth of 2500 m occurs after the tensile failure of the casing–cement interface which is still prior to the time step one (before 30 days). In fact, the cement-rock interface loses its durability due to the early invasion of CO_2-bearing fluids and will be converted to a potential zone subject to failure due to the shear stress. Calculations in this paper show that the stresses in the r-direction and the θ-direction are similar, while the difference between them and the stress in the z-direction increases with the depth. In addition, the early degradation of the cement sheath due to CO_2 attack at the locations nearby the injection points increases the tendency of the cement sheath to fail due to both the increased shear stress and the low strength of the outermost layers of the cement sheath.

Table 6. The status of the ITZs at the time step of zero for a well used for CO_2 injection for 2.5 years which is abandoned afterwards. (N: the ITZ is in the elastic zone and intact)

Depth (m)	**The type of band**	
	The casing-cement interface	**The cement-rock interface**
800	N	N
1140	N	N
1480	PDB	N
1820	PDB	N
2160	PDB	N
2500	PDB	DSB

Figure 13 (a) and Table 6 show that the casing-cement interface will never suffer a shear failure. The casing-cement interface at shallower depths (800 and 1140 m) remains safe while at the deeper locations it fails due to the tensile stress created by the increasing temperature difference between the injection fluid and the formation. At deeper locations, the temperature of formation is higher than that at shallower depths while the temperature of injected CO_2 remains around 30℃. This results in a larger temperature difference at deeper locations. This process reduces the UTS of the casing-cement interface to a very small value, ε_2, as represented in Flowchart A.2 in supplementary data. This is the reason for a significant reduction in η_t at depths greater than 1140 m. Figure 13 explains that after forming PDBs at the casing-cement interface in deep points of the well, the effect of the tensile stress, which is created by a reduction in the temperature in the well, diminishes. This is due to the inability of the casing-cement interface to transmit the tensile stress. Actually, the casing is separated from the cement sheath; therefore the pulling force, which is created due to tensile stress, on the each end-sides of the casing-cement assemblage will not affect the other side. This case is included in Flowchart A.2 (acts 18-19) and Flowchart A.3 (acts 14-15). The *in-situ* horizontal stress from the surrounding formations pushes the cement sheath back to the casing wall. In fact, in the next time steps, the compressive stress will act on this interface, leading to a remarkable decrease in η_t. It is worth noting that there is already a gap at the casing-cement interface which can be converted into an escaping pathway for CO_2-bearing fluids.

Figure 14 (c) shows that the cement-rock interface will be compacted at all depths after 200 days. It can be observed in Figure 14 (a) that the value of η_s for depths of 800, 1140, and 2500 m becomes larger than or equal to one before the 200th day. At these depths, based on the formation of DSBs at the cement-rock interface, the value of UTS decrease to ε_2 because the cement-rock interface fails and is not able to withstand any value of the tensile stress. This is the reason for a remarkable reduction in the value of η_t at these depths in Figure 14 (b). Furthermore, at the middle depth ranges of 1480, 1820, and 2160 m the cement-rock interface remains intact although Figure 14 (a) shows that there is a high potential for them to be dilated i.e., to fail due to the shear stress. It can be inferred that the cement-rock interface at the locations near the injection points will be dilated due to the shear stress or close to the dilation shear process once CO_2 is injected. The entire cement sheath will retain its integrity due to a significant deceleration in the degrading process resulting from the carbonation and the compaction of the cement-rock interface, as represented in Figure 15. It can be understood from Figures 13-15 that in an injection-abandonment process, the casing-cement and the cement-rock interfaces will be dilated due to the tensile and the shear stresses, respectively. The DSB at the cement-rock interface is a potential leakage pathway depending on the porosity increase due to the shear dilation, however, it is not comparable with the casing-cement interface which will be converted to a highly conductive passage due to the formation of the PDB. It is a fortunate process that the compaction of the cement-rock interface will restrict the dilation effect by reducing the porosity to one order of magnitude at the affected zones.

As discussed in [29], the compaction process is a promising phenomenon which postpones the failure of the cement sheath. The compaction of the outermost layers of the cement sheath (or the cement-rock interface), as show in Figure 14 (c), decreases the porosity. In addition, the carbonation process at locations close the cement-rock interface also leads to a decrease in the porosity. These two processes prevent further invasion of the carbon species deep into the cement sheath. Therefore, as shown in Figure 15, the failure criteria have no significant upward trends from which we can interpret that the cement sheath will not fail in the near future. The extrapolation of trends in Figures 13-15 shows the lifespans of the ITZs and the cement sheath as outlined in Figure 16. It can be understood from this figure that the casing-cement interface fails due to the pure dilation process at depths deeper than 1140 m once CO_2 is injected. This means a complete separation of the cement sheath from the casing outer face occurs due to a significant increase in the temperature drop. The well temperature decreases from the temperature of the formation to the CO_2 injection temperature of 30 ℃. The reduction in the temperature of the rock-cement-casing assemblage increases with depth. The shear dilation process results in a failing of the cement-rock interface at depths shallower than 1140 m and depths deeper than 2245 m. At depths between 1225 and 2160 m, the cement-rock interface is not expected to fail due to the shear dilation as shown in Figure 16. On the other hand, Figure 14 (a) shows that the cement-rock interface becomes extremely close to failure due to the shear dilation. The authors believe that the cement-rock interface is also subject to the shear dilation at the depths between 1225 and 2160 m. Therefore, with increasing in depth the cement-rock interface fails due to the shear dilation. This process becomes faster with depth due to increasing in the *in-situ* horizontal stress, and

the dissolution of higher quantities of carbon species accelerating the degredation process of the cement matrix. The cement-rock interface at the entire range of 800-2500 m is compacted as can be observed in Figure 16. In this case study, the cement sheath remains intact.

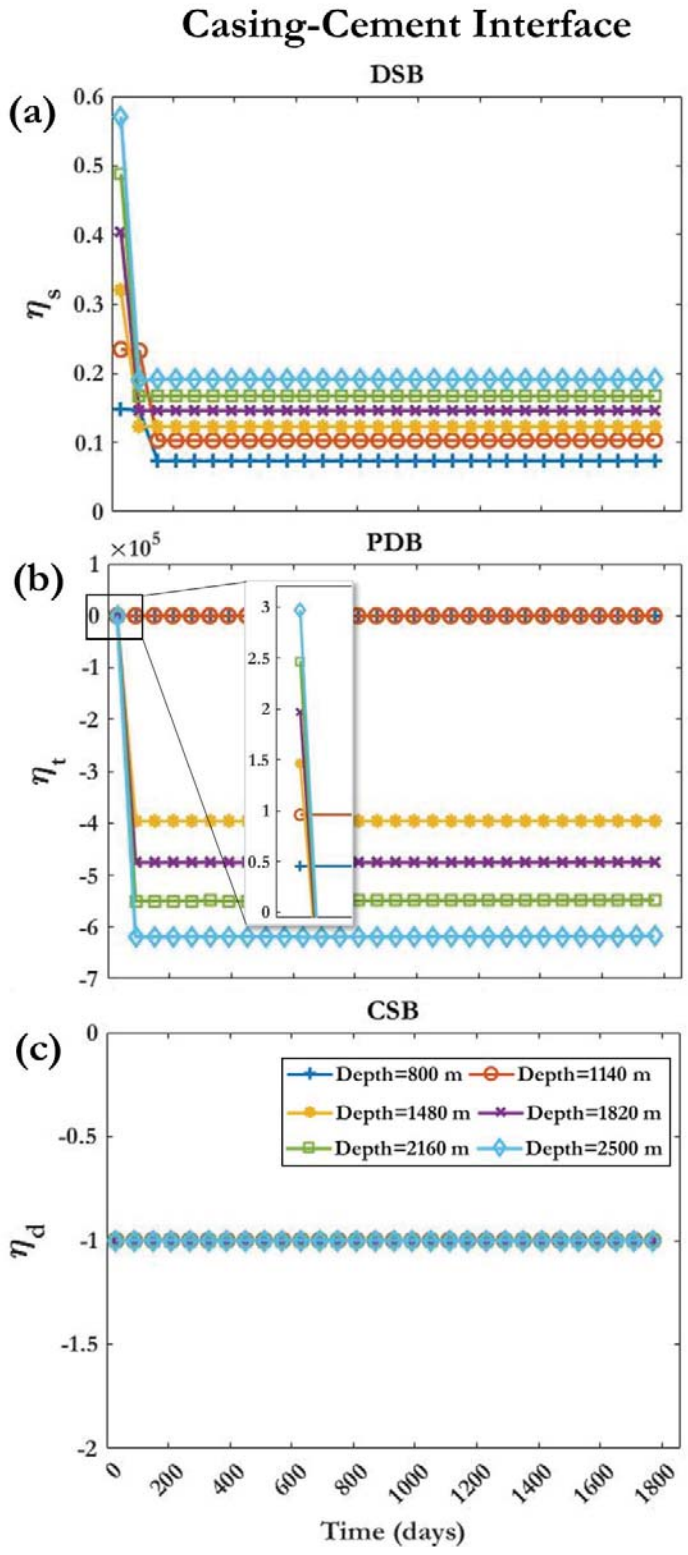

Figure 13. (a) Change in the value of the shear failure criterion, η_s; (b) the tensile failure criterion, η_t; (c) and the deformation criterion, η_d, at different depths for the casing-cement interfacial transition zone for a well used for CO_2 injection for 2.5 years and then abandoned.

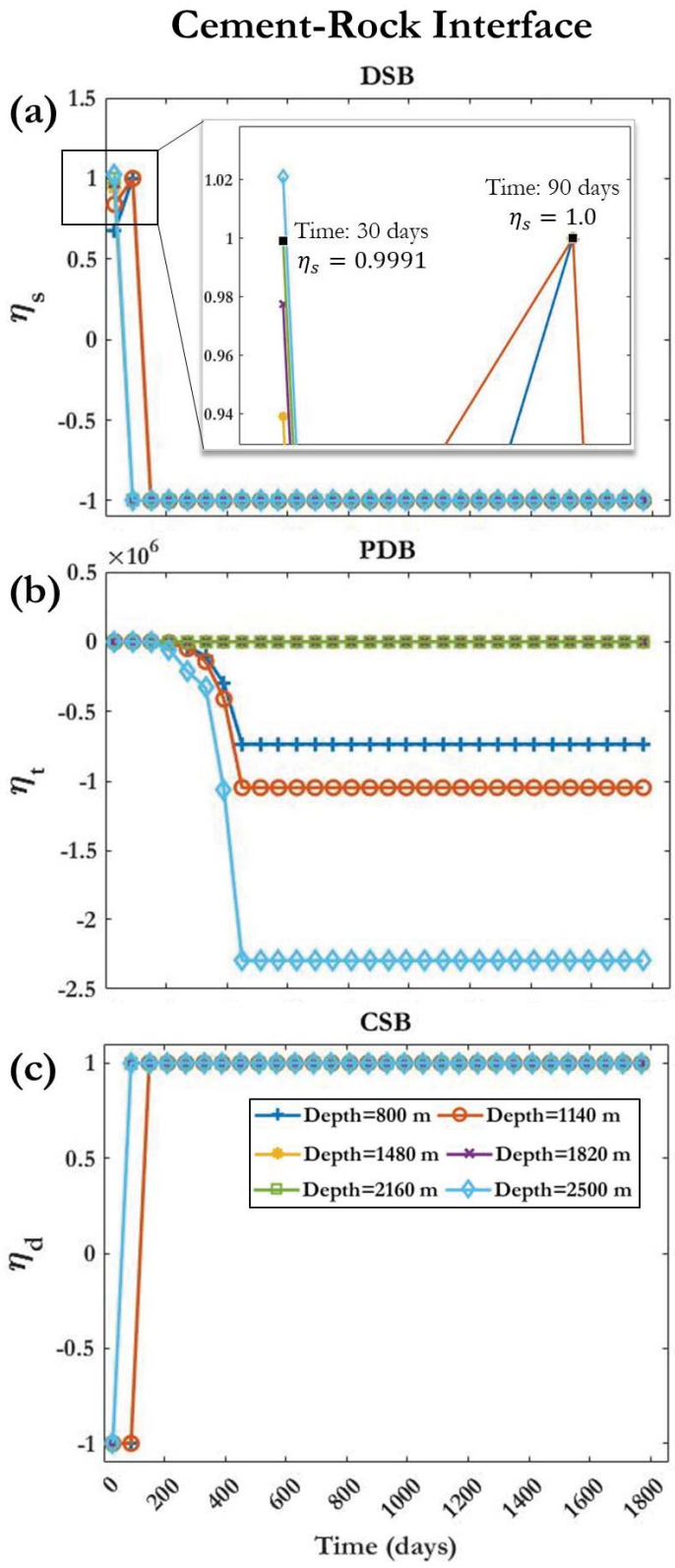

Figure 14. (a) Change in the value of the shear failure criterion, η_s; (b) the tensile failure criterion, η_t; (c) and the deformation criterion, η_d, at different depths for the cement-rock interfacial transition zone for a well used for CO_2 injection for 2.5 years and then abandoned.

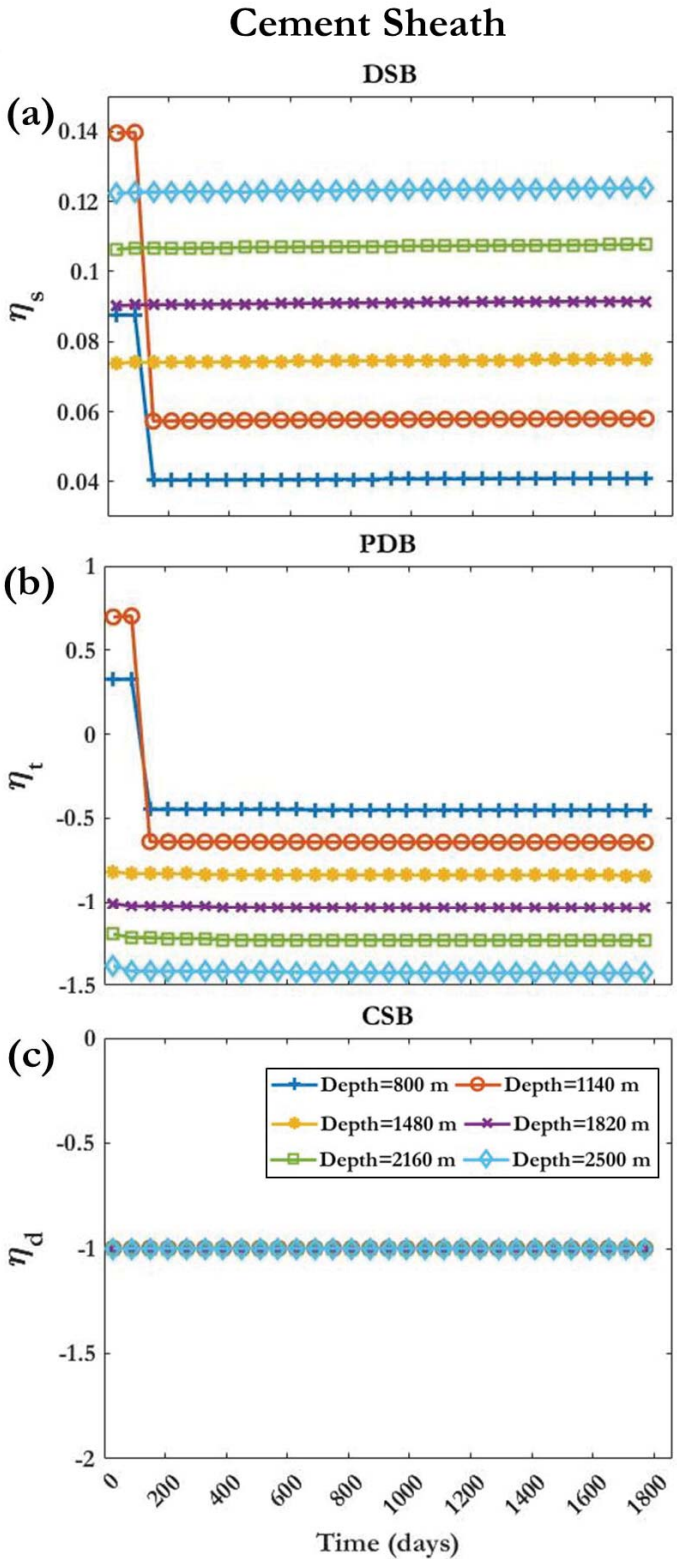

Figure 15. (a) Change in the value of the shear failure criterion, η_s; (b) the tensile failure criterion, η_t; (c) and the deformation criterion, η_d, at different depths for the entire cement sheath for a well used for CO_2 injection for 2.5 years and then abandoned.

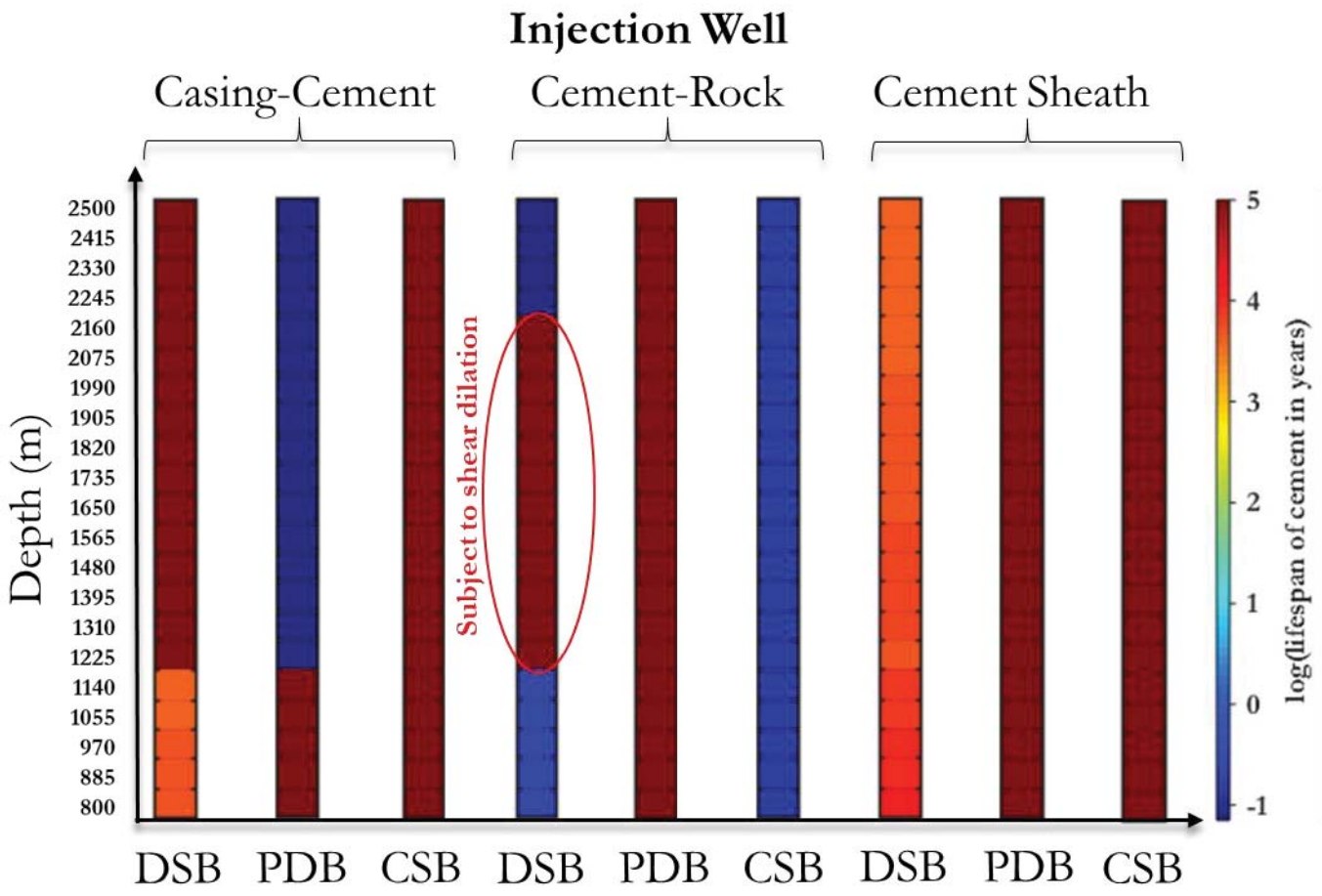

Figure 16. The lifespan of the casing-cement and cement-rock interfaces, and the cement sheath for an injection well which abandoned after 2.5 years of being used for CO_2 injection.

9. Conclusions

This study provides a methodology for investigating the behaviour of the rock-cement-casing assemblage in CO_2 storage sites. A plastic-damage model is introduced to capture the effect of the inelastic behaviour of the cement matrix. The alteration of the cement matrix is characterised as a function of both the failure and the deformation in the inelastic area. The concept of bands is coupled with the plastic-damage model to explicitly involve the effect of the alteration in the cement structure on porosity in the inelastic area. The geochemistry calculations have been undertaken using the CrunchFlow code. The mechanical calculations are coupled with the geochemical alterations in an iterative approach which continuously updates the boundary conditions based on the solidity and the stress state of ITZs. The assumptions of the complete dissolution of CO_2 in brine and the single-phase dominance of CO_2-bearing fluids in the pores of the cement matrix makes the geochemical alterations independent of the mechanical calculations. Therefore, the suggested iterative approach in this work is a reasonable method in terms of the numerical aspects, however, the coupled calculations may be completed in a longer period of time compared to the fully implicit methods.

A uniaxial plastic-damage approach is adopted in this paper to avoid the complexity and computational expense which is associated with implementing triaxial plastic-damage models. The constant parameters describing the failure envelope are subject to alteration due to the chemical reactions and the effect of the stress state. Although we tried to model the alteration in these parameters (such as compressive and tensile strengths and the Young's modulus) and porosity, their simultaneous evolution has not been validated in this paper, and their investigations require further studies and experiments. Modelling the vertical movement of CO_2 was also beyond the purpose of this paper and needs further work.

For an abandoned well, no failure (PDB and DSB) is expected to occur at the ITZs and in the cement sheath. The cement-rock interface will be compacted due to the *in-situ* horizontal stress and the shrinkage of the cap surface resulting from the chemical degradation. The compaction deforms the cement-rock interface but does not lead to failure. Although the cement-rock interface deforms, its strength remains a function of the minimum UCS which has been reached. It should be noted that the maximum cohesive strength between two solids is assumed to be a function of their chemistry. This strength can only be degraded due to mechanical alterations. Indeed, the cohesive strength is not expected to surpass the maximum value which is achievable based on the chemical composition of two adjacent surfaces. The compressive stress can keep two solids beside each other but is not able to improve the maximum achievable cohesive strength. Therefore, an abandoned well will remain safe for an infinite length of time.

In the injection wells, the temperature difference between the injected fluid and the rock results in the formation of tensile stress in the rock-cement-casing assemblage. This tensile stress at the early stages of CO_2 injection (before 30 days) leads to the failure of the casing-cement interface. This failure is an annular space around the casing with a porosity of one. Early on in the injection phase, prior to the 200th day, the cement-rock interface faces a shear failure which is a result of an increase in the difference between the stress in the z-direction, σ_z, and the stresses in the r-direction, σ_r, and the θ-direction, σ_θ. Although the DSB at the cement-rock interface increases the porosity by 8%, the compaction of this layer after 200 days, however, restricts this effect. Generally, the gap created at the casing-cement interface will provide a high conductive leakage pathway if CO_2-bearing fluids find a way into that zone. For an injection well, the cement sheath will be separated from the rock and the casing surfaces after 200 days and the *in-situ* horizontal stress will keep them as an assemblage. The carbonation process and the formation of CSB accompanied by a reduction in the porosity value will limit both the tendency of the CO_2 to escape from the ITZs and the diffusion of CO_2-bearing fluid into deeper locations within the cement sheath. Overall, CO_2 injection will result in the formation of PDB and DSB at the casing-cement and the cement-rock interfaces, respectively. Under normal conditions, however, their performance as the leakage pathways will be restricted due the carbonation process and the formation of CSB at the cement-rock interface.

Acknowledgements

We appreciate the Research Centre for Fluid and Complex Systems (FCS) and the Research Centre for Built and Natural Environment (BNE) at Coventry University for their financial

support. The authors also would like to show their gratitude to the staff at these two centres for supporting this work through their invaluable comments, especially Dr Philip Costen who kindly helps us in improving the manuscript. We also thank Dr Carl Steefel for the use of the CrunchFlow code.

References

[1] H. Abdoulghafour, P. Gouze, L. Luquot, R. Leprovost, Characterization and modeling of the alteration of fractured class-G Portland cement during flow of CO2-rich brine, Int. J. Greenh. Gas Control. 48 (2016) 155–170. https://doi.org/10.1016/j.ijggc.2016.01.032.

[2] J.W. Carey, M. Wigand, S.J. Chipera, G. WoldeGabriel, R. Pawar, P.C. Lichtner, S.C. Wehner, M.A. Raines, G.D. Guthrie, Analysis and performance of oil well cement with 30 years of CO2 exposure from the SACROC Unit, West Texas, USA, Int. J. Greenh. Gas Control. 1 (2007) 75–85. https://doi.org/10.1016/S1750-5836(06)00004-1.

[3] S. Carroll, J.W. Carey, D. Dzombak, N.J. Huerta, L. Li, T. Richard, W. Um, S.D.C. Walsh, L. Zhang, Review: Role of chemistry, mechanics, and transport on well integrity in CO2storage environments, Int. J. Greenh. Gas Control. 49 (2016) 149–160. https://doi.org/10.1016/j.ijggc.2016.01.010.

[4] J. Corvisier, A. Fabbri, F. Brunet, Y. Leroy, B. Goffé, G. Rimmelé, V. Barlet-Gouédard, A Numerical Model for CO_2 Wells Ageing through Water/Supercritical CO_2 /Cement Interactions, in: Thermo-Hydromechanical Chem. Coupling Geomaterials Appl., John Wiley & Sons, Inc., Hoboken, NJ, USA, 2013: pp. 75–84. https://doi.org/10.1002/9781118623565.ch5.

[5] A. Duguid, M. Radonjic, G.W. Scherer, Degradation of cement at the reservoir/cement interface from exposure to carbonated brine, Int. J. Greenh. Gas Control. 5 (2011) 1413–1428. https://doi.org/10.1016/j.ijggc.2011.06.007.

[6] A. Duguid, G.W. Scherer, Degradation of oilwell cement due to exposure to carbonated brine, Int. J. Greenh. Gas Control. 4 (2010) 546–560. https://doi.org/10.1016/j.ijggc.2009.11.001.

[7] N.J. Huerta, S.L. Bryant, B.R. Strazisar, B.G. Kutchko, L.C. Conrad, The influence of confining stress and chemical alteration on conductive pathways within wellbore cement, Energy Procedia. 1 (2009) 3571–3578. https://doi.org/10.1016/j.egypro.2009.02.151.

[8] N. Hyvert, A. Sellier, F. Duprat, P. Rougeau, P. Francisco, Dependency of C-S-H carbonation rate on CO2 pressure to explain transition from accelerated tests to natural carbonation, Cem. Concr. Res. 40 (2010) 1582–1589. https://doi.org/10.1016/j.cemconres.2010.06.010.

[9] A. Raoof, H.M. Nick, T.K.T. Wolterbeek, C.J. Spiers, Pore-scale modeling of reactive transport in wellbore cement under CO2 storage conditions, Int. J. Greenh. Gas Control. 11 (2012) 67–77. https://doi.org/10.1016/j.ijggc.2012.09.012.

[10] G. Rimmelé, V. Barlet-Gouédard, O. Porcherie, B. Goffé, F. Brunet, Heterogeneous porosity distribution in Portland cement exposed to CO2-rich fluids, Cem. Concr. Res.

38 (2008) 1038–1048. https://doi.org/10.1016/j.cemconres.2008.03.022.

[11] W. Ashraf, Carbonation of cement-based materials: Challenges and opportunities, Constr. Build. Mater. 120 (2016) 558–570. https://doi.org/10.1016/j.conbuildmat.2016.05.080.

[12] K. Nakano, A. Ohbuchi, S. Mito, Z. Xue, Chemical interaction of well composite samples with supercritical CO2 along the cement - Sandstone interface, Energy Procedia. 63 (2014) 5754–5761. https://doi.org/10.1016/j.egypro.2014.11.608.

[13] A. Fabbri, J. Corvisier, A. Schubnel, F. Brunet, B. Goffé, G. Rimmele, V. Barlet-Gouédard, Effect of carbonation on the hydro-mechanical properties of Portland cements, Cem. Concr. Res. 39 (2009) 1156–1163. https://doi.org/10.1016/j.cemconres.2009.07.028.

[14] M. Zhang, S. Bachu, Review of integrity of existing wells in relation to CO2 geological storage: What do we know?, Int. J. Greenh. Gas Control. 5 (2011) 826–840. https://doi.org/10.1016/j.ijggc.2010.11.006.

[15] J.P.L. Brunet, L. Li, Z.T. Karpyn, B.G. Kutchko, B. Strazisar, G. Bromhal, Dynamic evolution of cement composition and transport properties under conditions relevant to geological carbon sequestration, Energy and Fuels. 27 (2013) 4208–4220. https://doi.org/10.1021/ef302023v.

[16] N.J. Huerta, S.L. Bryant, L. Conrad, Cement Core Experiments With A Conductive Leakage Pathway , Under Confining Stress And Alteration Of Cement ' s Mechanical Properties Via A Reactive Fluid , As An Analog For CO2 Leakage Scenario, SPE/DOE Improv. Oil Recover. Symp. Tulsa, Oklahoma, 19-23 April. SPE-113375 (2008). https://doi.org/10.2118/113375-MS.

[17] B.G. Kutchko, B.R. Strazisar, D.A. Dzombak, G. V Lowry, N. Thaulow, Degradation of Well Cement by CO2 under Geological Sequestration Conditions, Env. Sci Technol. 41 (2007) 4787–4792. https://doi.org/10.1021/es062828c.

[18] B. Lecampion, J. Vanzo, F.-J. Ulm, B. Huet, C. Germay, I. Khalfallah, J. Dirrenberger, Evolution of Portland Cement Mechanical Properties Exposed To Co2-Rich Fluids: Investigation At Different Scales, MPPS 2011, Symp. Mech. Phys. Porous Solids A Tribut. to Pr. Oliv. Coussy. (2011) 1–24.

[19] S.D.C. Walsh, H.E. Mason, W.L. Du Frane, S.A. Carroll, Mechanical and hydraulic coupling in cement-caprock interfaces exposed to carbonated brine, Int. J. Greenh. Gas Control. 25 (2014) 109–120. https://doi.org/10.1016/j.ijggc.2014.04.001.

[20] L. Zhang, D.A. Dzombak, D. V. Nakles, J.P.L. Brunet, L. Li, Reactive transport modeling of interactions between acid gas (CO 2 + H2S) and pozzolan-amended wellbore cement under geologic carbon sequestration conditions, Energy and Fuels. 27 (2013) 6921–6937. https://doi.org/10.1021/ef401749x.

[21] J.W. Carey, R. Svec, R. Grigg, J. Zhang, W. Crow, Experimental investigation of wellbore integrity and CO2-brine flow along the casing-cement microannulus, Int. J. Greenh. Gas Control. 4 (2010) 272–282. https://doi.org/10.1016/j.ijggc.2009.09.018.

[22] J. Won, H.-J. Choi, H. Lee, H. Choi, Numerical Investigation on the Effect of Cementing Properties on the Thermal and Mechanical Stability of Geothermal Wells, Energies. 9

(2016) 1016. https://doi.org/10.3390/en9121016.

[23] J. Corvisier, F. Brunet, A. Fabbri, S. Bernard, N. Findling, G. Rimmelé, V. Barlet-Gouédard, O. Beyssac, B. Goffé, Raman mapping and numerical simulation of calcium carbonates distribution in experimentally carbonated Portland-cement cores, Eur. J. Mineral. 22 (2010) 63–74. https://doi.org/10.1127/0935-1221/2010/0022-1977.

[24] J. Iyer, S.D.C. Walsh, Y. Hao, S.A. Carroll, Incorporating reaction-rate dependence in reaction-front models of wellbore-cement/carbonated-brine systems, Int. J. Greenh. Gas Control. 59 (2017) 160–171. https://doi.org/10.1016/j.ijggc.2017.01.019.

[25] B.G. Kutchko, B.R. Strazisar, G.V. Lowry, D. a. Dzombak, N. Thaulow, Rate of CO2 Attack on Hydrated Class H Well Cement under Geologic Sequestration Conditions, Environ. Sci. \& Technol. 42 (2008) 6237–6242. https://doi.org/10.1021/es800049r.

[26] J. Liaudat, A. Martínez, C.M. López, I. Carol, Modelling acid attack of oilwell cement exposed to carbonated brine, Int. J. Greenh. Gas Control. 68 (2018) 191–202. https://doi.org/10.1016/j.ijggc.2017.11.015.

[27] O. Omosebi, H. Maheshwari, R. Ahmed, S. Shah, S. Osisanya, S. Hassani, G. DeBruijn, W. Cornell, D. Simon, Degradation of well cement in HPHT acidic environment: Effects of CO2concentration and pressure, Cem. Concr. Compos. 74 (2016) 54–70. https://doi.org/10.1016/j.cemconcomp.2016.09.006.

[28] M. Bagheri, S.M. Shariatipour, E. Ganjian, A review of oil well cement alteration in CO2-rich environments, Constr. Build. Mater. 186C (2018) 946–968. https://doi.org/10.1016/j.conbuildmat.2018.07.250.

[29] M. Bagheri, S.M. Shariatipour, E. Ganjian, Prediction of the lifespan of cement at a specific depth based on the coupling of geomechanical and geochemical processes for CO2 storage, Int. J. Greenh. Gas Control. 86 (2019) 43–65. https://doi.org/10.1016/j.ijggc.2019.04.016.

[30] M.R. McLean, M.A. Addis, Wellbore Stability Analysis: A Review of Current Methods of Analysis and Their Field Application, SPE/IADC Drill. Conf. 27 February-2 March, Houston, Texas. (1990).

[31] M.R. McLean, M.A. Addis, Wellbore Stability: The Effect of Strength Criteria on Mud Weight Recommendations, SPE Annu. Tech. Conf. Exhib. (1990). https://doi.org/10.2118/20405-MS.

[32] M. Yu, M.E. Chenevert, M.M. Sharma, Chemical-mechanical wellbore instability model for shales: Accounting for solute diffusion, J. Pet. Sci. Eng. 38 (2003) 131–143. https://doi.org/10.1016/S0920-4105(03)00027-5.

[33] R. Gholami, B. Aadnoy, N. Fakhari, A thermo-poroelastic analytical approach to evaluate cement sheath integrity in deep vertical wells, J. Pet. Sci. Eng. 147 (2016) 536–546. https://doi.org/10.1016/j.petrol.2016.09.024.

[34] R. Gholami, V. Rasouli, B. Aadnoy, M. Mohammadnejad, Geomechanical and numerical studies of casing damages in a reservoir with solid production, Rock Mech. Rock Eng. 49 (2016) 1441–1460. https://doi.org/10.1007/s00603-015-0828-5.

[35] W. Wang, A.D. Taleghani, Three-dimensional analysis of cement sheath integrity around Wellbores, J. Pet. Sci. Eng. 121 (2014) 38–51. https://doi.org/10.1016/j.petrol.2014.05.024.

[36] E. Arjomand, T. Bennett, G.D. Nguyen, Evaluation of cement sheath integrity subject to enhanced pressure, J. Pet. Sci. Eng. 170 (2018) 1–13. https://doi.org/10.1016/j.petrol.2018.06.013.

[37] H. Xu, N. Peng, T. Ma, B. Yang, Investigation of Thermal Stress of Cement Sheath for Geothermal Wells during Fracturing, Energies. 11 (2018) 2581. https://doi.org/10.3390/en11102581.

[38] H. Xu, T. Ma, N. Peng, B. Yang, Influences of Fracturing Fluid Injection on Mechanical Integrity of Cement Sheath under Four Failure Modes, Energies. 11 (2018) 3534. https://doi.org/10.3390/en11123534.

[39] Z. Zhang, H. Wang, Effect of thermal expansion annulus pressure on cement sheath mechanical integrity in HPHT gas wells, Appl. Therm. Eng. 118 (2017) 600–611. https://doi.org/10.1016/j.applthermaleng.2017.02.075.

[40] L. Zhang, X. Yan, X. Yang, X. Zhao, Evaluation of wellbore integrity for HTHP gas wells under solid-temperature coupling using a new analytical model, J. Nat. Gas Sci. Eng. 25 (2015) 347–358. https://doi.org/10.1016/j.jngse.2015.05.023.

[41] M. Bagheri, S.M. Shariatipour, E. Ganjian, A Study on the Chemo-mechanical Alteration of Cement in CO2 Storage Sites, SPE Eur. Featur. 81st EAGE Annu. Conf. Exhib. SPE-195520 (2019).

[42] Y. Xiao, Z. Chen, J. Zhou, Y. Leng, R. Xia, Concrete plastic-damage factor for finite element analysis: Concept, simulation, and experiment, Adv. Mech. Eng. 9 (2017) 1–10. https://doi.org/10.1177/1687814017719642.

[43] P. Grassl, D. Xenos, U. Nyström, R. Rempling, K. Gylltoft, CDPM2: A damage-plasticity approach to modelling the failure of concrete, Int. J. Solids Struct. 50 (2013) 3805–3816. https://doi.org/10.1016/j.ijsolstr.2013.07.008.

[44] E. Hoek, E.T. Brown, Practical estimates of rock mass strength, Int. J. Rock Mech. Min. Sci. 34 (1997) 1165–1186. https://doi.org/10.1016/S1365-1609(97)80069-X.

[45] M.A. Biot, Theory of elasticity and consolidation for a porous anisotropic solid, J. Appl. Phys. 26 (1955) 182–185. https://doi.org/10.1063/1.1721956.

[46] V.I. Osipov, Physicochemical theory of effective stress in soils, Physicochem. Theory Eff. Stress Soils. (2015) 1–55. https://doi.org/10.1007/978-3-319-20639-4.

[47] K. Terzaghi, Theoretical Soil Mechanics, (1943). https://doi.org/10.1002/9780470172766.

[48] J. Geertsma, The effect of fluid pressure decline on volumetric changes of porous rocks, Trans Am Inst Min Met. Pet Eng. 210 (1957) 331–340.

[49] A.W. Skempton, Effective Stress in Soils, Concrete and Rocks, in: Sel. Pap. SOIL Mech., Thomas Telford Publishing, 1984: pp. 106–118.

https://doi.org/10.1680/sposm.02050.0014.

[50] A. Nur, J.D. Byerlee, An exact effective stress law for elastic deformation of rock with fluids, J. Geophys. Res. 76 (1971) 6414–6419. https://doi.org/10.1029/JB076i026p06414.

[51] M.H. Sadd, Elasticity. Theory, Applications, and Numerics, 2005.

[52] P. Maimí, P.P. Camanho, J.A. Mayugo, C.G. Dávila, A continuum damage model for composite laminates: Part I - Constitutive model, Mech. Mater. 39 (2007) 897–908. https://doi.org/10.1016/j.mechmat.2007.03.005.

[53] H. Jo, K.E. Gray, Mechanical Behavior of Concentric Casing, Cement, And Formation Using Analytical And Numerical Methods, (2010). https://www.onepetro.org/conference-paper/ARMA-10-142 (accessed February 18, 2019).

[54] M. De Simone, F.L.G. Pereira, D.M. Roehl, Analytical methodology for wellbore integrity assessment considering casing-cement-formation interaction, Int. J. Rock Mech. Min. Sci. 94 (2017) 112–122. https://doi.org/10.1016/j.ijrmms.2016.12.002.

[55] O. Omidi, V. Lotfi, Numerical Analysis of Cyclically Loaded Concrete Under Large Tensile Strains by the Plastic-Damage Model, Trans. A Civ. Eng. 17 (2010) 194–208.

[56] S. Zhou, R. Liu, H. Zeng, Y. Zeng, L. Zhang, J. Zhang, X. Li, Mechanical characteristics of well cement under cyclic loading and its influence on the integrity of shale gas wellbores, Fuel. 250 (2019) 132–143. https://doi.org/10.1016/j.fuel.2019.03.131.

[57] J. Lubliner, J. Oliver, S. Oller, E. Oñate, A plastic-damage model for concrete, Int. J. Solids Struct. 25 (1989) 299–326. https://doi.org/10.1016/0020-7683(89)90050-4.

[58] J. Lee, G.L. Fenves, Plastic-Damage Model for Cyclic Loading of Concrete Structures, J. Eng. Mech. 124 (1998) 892–900. https://doi.org/10.1061/(ASCE)0733-9399(1998)124:8(892).

[59] J.F. Sima, P. Roca, C. Molins, Cyclic constitutive model for concrete, Eng. Struct. 30 (2008) 695–706. https://doi.org/10.1016/J.ENGSTRUCT.2007.05.005.

[60] B.D.Z. Yankelevsky, H.W. Reinhardt, Model for cyclic compressive behavior of concrete, 113 (1987) 228–240.

[61] B.Y. Bahn, C.T.T. Hsu, Stress-strain behavior of concrete under cyclic loading, ACI Mater. J. 95 (1998) 178–193.

[62] I. Karsan, J. JO, Behavior of concrete under compressive loadings, ASCE J. Struct. Eng. 95 (1969) 2543–2563. https://trid.trb.org/view/105607 (accessed October 3, 2019).

[63] J. Zhao, Applicability of Mohr-Coulomb and Hoek-Brown strength criteria to the dynamic strength of brittle rock, Int. J. Rock Mech. Min. Sci. 37 (2000) 1115–1121. https://doi.org/10.1016/S1365-1609(00)00049-6.

[64] A. Aydin, R.I. Borja, P. Eichhubl, Geological and mathematical framework for failure modes in granular rock, J. Struct. Geol. 28 (2006) 83–98. https://doi.org/10.1016/j.jsg.2005.07.008.

[65] D.C. Drucker, W. Prager, SOIL MECHANICS AND PLASTIC ANALYSIS OR LIMIT DESIGN, Q. Appl. Math. 10 (1952) 157–165. https://pdfs.semanticscholar.org/6583/be285aef2087223d19e890c8d94aa8a89805.pdf (accessed November 8, 2018).

[66] P. Rochette, P. Labossiere, A Plasticity Approach for Concrete Columns Confined with Composite Materials, Adv. Compos. Mater. Bridg. Struct. -INTERNATIONAL Conf. (1996) 359–366. https://www.tib.eu/en/search/id/BLCP%3ACN018623351/A-Plasticity-Approach-for-Concrete-Columns-Confined/#documentinfo (accessed January 22, 2019).

[67] E. Bemer, O. Vincké, P. Longuemare, Geomechanical log deduced from porosity and mineralogical content, Oil Gas Sci. Technol. 59 (2004) 405–426. https://doi.org/10.2516/ogst:2004028.

[68] V.A. Lubarda, S. Mastilovic, J. Knap, Brittle-Ductile Transition in Porous Rocks by Cap Model, J. Eng. Mech. 122 (1996) 633–642. https://doi.org/10.1061/(asce)0733-9399(1996)122:7(633).

[69] T. Wong, C. David, W. Zhu, The transition from brittle faulting to cataclastic flow in porous sandstones: Mechanical deformation, J. Geophys. Res. Solid Earth. 102 (1997) 3009–3025. https://doi.org/10.1029/96jb03281.

[70] W. Zhu, T. Wong, The transition from brittle faulting to cataclastic flow: Permeability evolution, J. Geophys. Res. Solid Earth. 102 (1997) 3027–3041. https://doi.org/10.1029/96jb03282.

[71] H. Jiang, J. Zhao, Calibration of the continuous surface cap model for concrete, Finite Elem. Anal. Des. 97 (2015) 1–19. https://doi.org/10.1016/j.finel.2014.12.002.

[72] H. Fossen, R.A. Schultz, Z.K. Shipton, K. Mair, Deformation bands in sandstone: a review, J. Geol. Soc. London. 164 (2007) 755–769. https://doi.org/10.1144/0016-76492006-036.

[73] H. Fossen, Geometric analysis and scaling relations of deformation bands in porous sandstone, 19 (1997).

[74] H. Fossen, R. Soliva, G. Ballas, B. Trzaskos, C. Cavalcante, R.A. Schultz, A review of deformation bands in reservoir sandstones: geometries, mechanisms and distribution, Geol. Soc. London, Spec. Publ. 459 (2018) 9–33. https://doi.org/10.1144/sp459.4.

[75] H. Fossen, A. Bale, Deformation bands and their influence on fluid flow, Am. Assoc. Pet. Geol. Bull. 91 (2007) 1685–1700. https://doi.org/10.1306/07300706146.

[76] X. Du Bernard, P. Eichhubl, A. Aydin, Dilation bands: A new form of localized failure in granular media, Geophys. Res. Lett. 29 (2002) 29-1-29–4. https://doi.org/10.1029/2002gl015966.

[77] Y. Hamiel, V. Lyakhovsky, A. Agnon, Coupled evolution of damage and porosity in poroelastic media: Theory and applications to deformation of porous rocks, Geophys. J. Int. 156 (2004) 701–713. https://doi.org/10.1111/j.1365-246X.2004.02172.x.

[78] R.A. Schultz, R. Siddharthan, A general framework for the occurrence and faulting of

deformation bands in porous granular rocks, Tectonophysics. 411 (2005) 1–18. https://doi.org/10.1016/j.tecto.2005.07.008.

[79] R.A. Schultz, R. Soliva, H. Fossen, C.H. Okubo, D.M. Reeves, Dependence of displacement-length scaling relations for fractures and deformation bands on the volumetric changes across them, J. Struct. Geol. 30 (2008) 1405–1411. https://doi.org/10.1016/j.jsg.2008.08.001.

[80] D.R. Faulkner, C.A.L. Jackson, R.J. Lunn, R.W. Schlische, Z.K. Shipton, C.A.J. Wibberley, M.O. Withjack, A review of recent developments concerning the structure, mechanics and fluid flow properties of fault zones, J. Struct. Geol. 32 (2010) 1557–1575. https://doi.org/10.1016/j.jsg.2010.06.009.

[81] M.H. Anders, S.E. Laubach, C.H. Scholz, Microfractures: A review, J. Struct. Geol. 69 (2014) 377–394. https://doi.org/10.1016/j.jsg.2014.05.011.

[82] C.I. Steefel, C.A.J. Appelo, B. Arora, D. Jacques, T. Kalbacher, O. Kolditz, V. Lagneau, P.C. Lichtner, K.U. Mayer, J.C.L. Meeussen, S. Molins, D. Moulton, H. Shao, J. Šimůnek, N. Spycher, S.B. Yabusaki, G.T. Yeh, Reactive transport codes for subsurface environmental simulation, 2015. https://doi.org/10.1007/s10596-014-9443-x.

[83] J.P.L. Brunet, L. Li, Z.T. Karpyn, N.J. Huerta, Fracture opening or self-sealing: Critical residence time as a unifying parameter for cement-CO2-brine interactions, Int. J. Greenh. Gas Control. 47 (2016) 25–37. https://doi.org/10.1016/j.ijggc.2016.01.024.

[84] N.J. Huerta, M.A. Hesse, S.L. Bryant, B.R. Strazisar, C. Lopano, CO2-saturated water in a cement fracture : Application to wellbore leakage during geologic CO2 storage, 44 (2016) 276–289.

[85] B.M. Huet, J.H. Prevost, G.W. Scherer, Quantitative reactive transport modeling of Portland cement in CO2-saturated water, Int. J. Greenh. Gas Control. 4 (2010) 561–574. https://doi.org/10.1016/j.ijggc.2009.11.003.

[86] J. Shen, P. Dangla, M. Thiery, Reactive transport modeling of CO2 through cementitious materials under CO2 geological storage conditions, Int. J. Greenh. Gas Control. 18 (2013) 75–87. https://doi.org/10.1016/j.ijggc.2013.07.003.

[87] C. Geloni, T. Giorgis, A. Battistelli, Modeling of Rocks and Cement Alteration due to CO2Injection in an Exploited Gas Reservoir, Transp. Porous Media. 90 (2011) 183–200. https://doi.org/10.1007/s11242-011-9714-0.

[88] B. Huet, R. Fuller, J. Prevost, Development of a coupled geochemical transport code to simulate cement degradation in CO2 saturated brine, Eighth Int. Conf. Greenh. Gas Control Technol. June 19-22, 2006, Trondheim, Norw. (2006).

[89] S.D.C. Walsh, H.E. Mason, W.L. Du Frane, S.A. Carroll, Experimental calibration of a numerical model describing the alteration of cement/caprock interfaces by carbonated brine, Int. J. Greenh. Gas Control. 22 (2014) 176–188. https://doi.org/10.1016/j.ijggc.2014.01.004.

[90] S.D.C. Walsh, W.L. Du Frane, H.E. Mason, S.A. Carroll, Permeability of wellbore-cement fractures following degradation by carbonated brine, Rock Mech. Rock Eng. 46 (2013) 455–464. https://doi.org/10.1007/s00603-012-0336-9.

[91] N. Spycher, K. Pruess, J. Ennis-King, CO2-H2O mixtures in the geological sequestration of CO2. I. Assessment and calculation of mutual solubilities from 12 to 100°C and up to 600 bar, Geochim. Cosmochim. Acta. 67 (2003) 3015–3031. https://doi.org/10.1016/S0016-7037(03)00273-4.

[92] Z. Duan, R. Sun, An improved model calculating CO2 solubility in pure water and aqueous NaCl solutions from 273 to 533 K and from 0 to 2000 bar, Chem. Geol. 193 (2003) 257–271. https://doi.org/10.1016/S0009-2541(02)00263-2.

[93] O. Omosebi, MECHANICAL DEGRADATION OF WELL CEMENT IN HPHT CARBONIC ACID ENVIRONMENT: EXPERIMENTAL STUDIES AND MATHEMATICAL MODELING, 2016. https://doi.org/10.1017/CBO9781107415324.004.

[94] R. Ahmed, S. Shah, S. Osisanya, S. Hassani, O. Omosebi, R. Elgaddafi, H. Maheshwari, A. Srivastava, J. Hwang, M. Sharma, S. Tale, J. Jeon, EFFECT OF H2S AND CO2 IN HPHT WELLS ON TUBULARS AND CEMENT, 2015.

[95] E. Liteanu, C.J. Spiers, Fracture healing and transport properties of wellbore cement in the presence of supercritical CO2, Chem. Geol. 281 (2011) 195–210. https://doi.org/10.1016/j.chemgeo.2010.12.008.

[96] S. Mito, Z. Xue, H. Satoh, Experimental assessment of well integrity for CO<inf>2</inf> geological storage: Batch experimental results on geochemical interactions between a CO<inf>2</inf>-brine mixture and a sandstone-cement-steel sample, Int. J. Greenh. Gas Control. 39 (2015) 420–431. https://doi.org/10.1016/j.ijggc.2015.06.007.

[97] American Petroleum Institute, API Specification 10A - Specification for Cements and Materials for Well Cementing, (2002) 58.

[98] W. Liu, B. Yu, J. Deng, Analytical method for evaluating stress field in casing-cement-formation system of oil/gas wells, Appl. Math. Mech. (English Ed. 38 (2017) 1273–1294. https://doi.org/10.1007/s10483-017-2237-8.